Studying Energy and Electron Transfer Processes in Photosynthetic

Complexes Using Ultrafast Time-Resolved Optical Techniques


A Proposal


Submitted to the Advisory Committee


at


Purdue University


by


Naranbaatar Dashdorj


In Partial Fulfillment of the


Requirements for the


Preliminary Examination


April 2005

THE ADVISORY COMMITTEE

**Sergei Savikhin**

Assistant Professor of Physics and Biophysics

Principal Advisor of the Proposal

Chair of the Advisory Committee

**Albert W. Overhauser**

Stuart Distinguished Professor of Physics

Member of the Advisory Committee

**William A. Cramer**

Henry Koffler Distinguished Professor of Biological Sciences

Member of the Advisory Committee

**Stephen M. Durbin**

Professor of Physics and Biophysics

Associate Head of the Department of Physics

Member of the Advisory Committee

TABLE OF CONTENTS

LIST OF MANUSCRIPTS

This proposal is based on the following manuscripts:

**I.** **Electrochromic Shift of Chlorophyll Absorption in Photosystem I from _Synechocystis_ sp. PCC 6803: A Probe of Optical and Dielectric Properties around the Secondary Electron Acceptor**

**Naranbaatar Dashdorj**, Wu Xu, Peter Martinsson, Parag R. Chitnis and Sergei Savikhin, _Biophysical Journal_, **86**: 3121-3130 (2004).

**II.** **Asymmetric Electron Transfer in Cyanobacterial Photosystem I: Charge Separation and Secondary Electron Transfer Dynamics of Mutations near the Primary Electron Acceptor $A_0$**

**Naranbaatar Dashdorj**, Wu Xu, Rachel O. Cohen, John H. Golbeck and Sergei Savikhin, _Biophysical Journal_, **88**: 1238-1249 (2005).

**III.** **The Single Chlorophyll _a_ Molecule in the Cytochrome $b_6f$ Complex: Unusual Optical Properties Protect the Complex Against Singlet Oxygen**

**Naranbaatar Dashdorj**, Huamin Zhang, Hanyoup Kim, Jiusheng Yan, William A. Cramer and Sergei Savikhin, _Biophysical Journal_, **88**: 1-10 (2005).

**IV.** **Probing the Active Electron Transfer Branch in the Photosystem I Reaction Center from _Synechocystis_ sp. PCC 6803**

**Naranbaatar Dashdorj**, Wu Xu, Rachel O. Cohen, John H. Golbeck and Sergei Savikhin, _In_ Photosynthesis: Fundamental Aspects to Global Perspectives. Art van der Est and Doug Bruce, Editors, ACG Publishing, Lawrence, KS, U.S.A. 30-33 (2005).

**V.    Unusual Optical Properties of the Monomeric Chlorophyll *a* in the Cytochrome *b₆f* Complex of Oxygenic Photosynthesis**

**Naranbaatar Dashdorj**, Huamin Zhang, Hanyoup Kim, Jiusheng Yan, William A. Cramer and Sergei Savikhin, *In* Photosynthesis: Fundamental Aspects to Global Perspectives. Art van der Est and Doug Bruce, Editors, ACG Publishing, Lawrence, KS, U.S.A. 451-453 (2005).

**VI.    Evidence For Long Range Triplet Excited State Energy Transfer from the Chlorophyll *a* to β-carotene in the Cytochrome *b₆f* Complex of Oxygenic Photosynthesis**

Hanyoup Kim, **Naranbaatar Dashdorj**, Huamin Zhang, Jiusheng Yan, William A. Cramer and Sergei Savikhin, *In* Photosynthesis: Fundamental Aspects to Global Perspectives. Art van der Est and Doug Bruce, Editors, ACG Publishing, Lawrence, KS, U.S.A. in press.

**VII.    A Long Range Triplet Energy Transfer from the Chlorophyll *a* to β-carotene in the Cytochrome *b₆f* Complex of Oxygenic Photosynthesis**

Hanyoup Kim, **Naranbaatar Dashdorj**, Huamin Zhang, Jiusheng Yan, William A. Cramer and Sergei Savikhin, in preparation.

LIST OF FIGURES

# LIST OF ABBREVIATIONS

| | |
|---|---|
| $A_{-1}$ | accessory pigment of the PS I RC |
| $A_0$ | primary electron acceptor of the PS I RC |
| $A_1$ | secondary electron acceptor of the PS I RC |
| ADP | adenosine diphosphate |
| ATP | adenosine triphosphate |
| ATPase | ATP synthase |
| Car | carotenoid |
| $^3$Car* | triplet excited state of Car |
| CBB cycle | Calvin-Benson-Bassham cycle |
| Chl $a$ | chlorophyll $a$ |
| Chl* $a$ | singlet excited state of Chl $a$ |
| $^3$Chl* $a$ | triplet excited state of Chl $a$ |
| Cyt | cytochrome |
| Cyt $b_6f$ | cytochrome $b_6f$ |
| Cyt $bc_1$ | cytochrome $bc_1$ |
| EPR | electron paramagnetic resonance |
| ET | electron transfer |
| $F_A$ | terminal electron acceptor of PS I |
| $F_B$ | terminal electron acceptor of PS I |
| $F_X$ | terminal electron acceptor of PS I preceding $F_A$ and $F_B$ |
| GT | grana thylakoids |
| ISP | iron-sulfur protein |
| LHC I | light harvesting complex I |
| LHC II | light harvesting complex II |
| NADP | nicotinamide adenine dinucleotide phosphate |

| | |
|---|---|
| $NADP^+$ | oxidized form of NADP |
| NADPH | reduced form of NADP |
| $O_2$ | molecular oxygen |
| $O_2^*$ | singlet excited state of $O_2$ |
| OEC | oxygen evolving center of PS II |
| P680 | primary electron donor or special pair of PS II |
| P700 | primary electron donor or special pair of PS I |
| Pheo | pheophytin |
| $P_i$ | inorganic phosphate |
| PS I | photosystem I |
| PS II | photosystem II |
| PQ | plastoquinone |
| $PQH_2$ | plastoquinol or doubly reduced dihydroplastoquinone |
| RC | reaction center |
| ST | stroma thylakoids |
| TEM | thin-section transmission electron micrograph |
| WT | wild-type |

PROLOGUE TO PHOTOSYNTHESIS

Primary Engine of the Biosphere

Photosynthesis can be defined as the light-driven reduction of atmospheric carbon dioxide by water to energy-rich organic compounds. However, this reductionist definition of photosynthesis provides modest insinuation on the fundamental roles of photosynthesis in sustaining life. As we briefly examine the following central roles of photosynthesis, it will become indubitably clear that photosynthesis is the process on which the very existence of the biosphere depends inexorably.

*Oxygenic photosynthesis is the sole replenisher of oxygen in the atmosphere.* Photosynthesis can be classified into oxygenic and anoxygenic by its nature to produce molecular oxygen as a by-product. It was the advent of oxygenic photosynthesis, the primary subject matter of this proposal, which transformed the atmosphere of the earth from its primitive, reducing state containing virtually no free oxygen to the present form. During oxygenic photosynthesis, photosynthetic organisms absorb atmospheric carbon dioxide and water, fix it as a carbohydrate and discard oxygen to the atmosphere.

*Photosynthesis fuels life utilizing the ultimate source of energy, the sun.* In most living organisms, energy-rich carbohydrates are burned to liberate the energy needed to sustain life using oxygen taken from the atmosphere in the process of metabolism. However, humans and animals are heterotrophs—they can not synthesize their own carbohydrates from inorganic compounds. Thus, they have to consume carbohydrates provided by photosynthesis either directly or indirectly.

*Every organic carbon in living organisms is processed through photosynthesis.* Carbon is the fundamental building block of material in living organisms. Humans and

animals can not assimilate carbons, thus they utilize the consumed carbohydrates as carbon source, in which carbon is driven from atmospheric carbon dioxide in synthesis of carbohydrates during the process of photosynthesis.

*Photosynthesis is the creator of fossil fuels and biomass.* Our principal energy source, on which we are so heavily dependent, is hydrocarbon-containing natural resources such as coal, petroleum and natural gas. According to the biogenic theory, these fossil fuels are the altered remnants of plant matter and marine organisms in the Carboniferous Period between 345 and 280 million years ago deposited in sedimentary rocks. The energy stored in these materials was captured from the solar radiation through photosynthesis. Photosynthesis also provides a significant contribution to world energy resources by creating biomass such as fuel-wood and energy crops.

These fundamental roles of photosynthesis provide underlining rationale for the title of this prologue: Primary Engine of the Biosphere. In turn, it gives rather consequential cause for studying photosynthesis, on top of trying to understand this complex physico-chemical process out of virtuous curiosity.

It should be noted that the converted energy is eventually dissipated as heat from living organisms and it can not be recycled within the lifecycle of the biosphere. Therefore, one way energy flow originated from the sun is realized through photosynthesis, which has been ensued for millions of years. Nevertheless, there is fortunately still enough energy available from the sun for photosynthesis to proceed for many hundreds of millions of years.

CHAPTER 1. MOLECULAR MECHANISMS OF PHOTOSYNTESIS

This chapter begins with brief introduction to photosynthetic organisms and organelles. It is followed by formulation of the balanced equation of photosynthesis. In the subsequent section, we concisely introduce the overall architecture of the photosynthetic energy transducing chain, which involves four major protein complexes integrally embedded in the photosynthetic membrane, based on the available crystallographic structures. It sets the ground for succinct discussion on how this intricate physico-chemical process of photosynthesis is carried out in molecular level, in other words, how these bio-nano-machines function to transduce the light energy into the biochemical energy needed to sustain life. In the last two sections, the two major integral membrane protein complexes, exclusively studied in this proposal, are discussed in more detail in the context of the crystal structures and functional mechanisms, wherein also the issues we investigated for this proposal are briefly discussed in the subsections.

1.1. Photosynthetic Organisms and Organelles

A wide variety of organisms including the cyanobacteria, algae and plants carry out oxygenic photosynthesis. The cyanobacteria are the single group of photosynthetic bacteria that are capable of performing oxygenic photosynthesis (Bryant 1994). Algae are a large group of organisms, either unicellular or colonial, containing many cells, which are dominant photosynthetic life forms in aquatic habitats (Graham and Wilcox 2000). Plants are the most complex of all photosynthetic organisms.

All algae and plants contain the subcellular organelle known as the chloroplast in which photosynthesis is carried out. The chloroplast is evolutionally originated from a

cyanobacterial-like cell through a process known as endosymbiosis (Blankenship 2002). As shown in thin-section transmission electron micrograph (TEM) of a chloroplast from a mesophyll cell of *Zea mays* in Fig. 1.1, the chloroplasts are convex lens-shaped structures with dimensions of several microns. Internally, the chloroplasts contain an extensive continuous membrane system known as the thylakoid membrane network that is surrounded by a colorless aqueous matrix called the stroma.
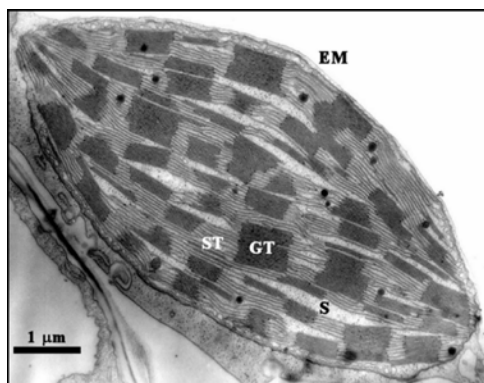


**Fig. 1.1** TEM of a chloroplast from a mesophyll cell of Zea mays (commonly known as sweet corn), showing compactly stacked grana (GT) and unstacked stroma (ST) regions of the thylakoid membrane in supporting matrix known as the stroma (S). Adapted with permission from (Archer and Barber 2004).

The three dimensional network of the thylakoid membrane encloses a single, anastomosing chamber, the thylakoid lumen. As the result, the thylakoid membrane network divides interior of a chloroplast into two compartments of stroma and lumen, introducing built-in asymmetry that is inherently important for the process of photosynthesis. The basic structure of the photosynthetic membrane and the molecular architecture of photosynthetic complexes are remarkably similar in all these organisms. In addition, the same underlining physical principles and molecular mechanism of photosynthesis are found throughout these organisms. It seems that the ability to carry out photosynthesis had optimized in the course of natural evolution several billion years ago to a degree where major alterations would not occur.

## 1.2. Equation of Photosynthesis

As briefly discussed in the prologue, photosynthesis literally means synthesis of energy-rich organic compounds utilizing light energy. Algae, cyanobacteria and plants synthesize mainly carbohydrates from two very simple inorganic molecules, water and carbon

dioxide, in which molecular oxygen is yielded as by-product. Thus, the equation of oxygenic photosynthesis can be characteristically written in the following simple form,

$$H_2O + CO_2 \xrightarrow{\text{hv}} (CH_2O) + O_2 \qquad\qquad (1.1)$$

In this minimally balanced equation, $CH_2O$ is representative of a carbohydrate.

## 1.3. Overall Architecture of Energy Transducing Chain

The synthesis process formulated in Eq. 1.1 or photosynthesis can be conceptually divided into two types of reactions: the directly light-driven reactions and the subsequent series of enzyme-catalyzed dark reactions. The directly light-driven reactions are mediated by the four major protein complexes that include photosystem I, photosystem II, ATP synthase and the cytochrome $b_6f$ complex (Cramer and Knaff 1990). These major protein complexes are integrally embedded in the thylakoid membrane with particular orientations such that they vectorially transport electrical charges in the form of electrons and protons across the membrane, generating an electrical as well as a chemical potential gradients used for the photosynthetic energy transduction. Highly selective permeability barrier that is osmotically intact is requisite in this energy conversion process. The thylakoid membrane, primarily formed by group of membrane lipids known as galactolipids, provides this functionally required feature. At the same time, the thylakoid membrane constitutes the architectural backbone of the photosynthetic energy transducing chain, in which rapid diffusion of lipophilic electron carriers and protein complexes are ensured as the result of its structurally cooperative nature.

Due to unwavering effort, meticulous hard work and commendable methodology of fellow scientists, the inclusive architectures of all protein complexes evolved in the energy transduction have been determined using X-ray crystallography. High-resolution crystal structure of cyanobacterial photosystem I (PS I) at 2.5 Å (Jordan et al. 2001) exposed an intricate architecture of this multisubunit membrane protein complex at atomic detail (Fig. 1.2). In addition, the X-ray crystal structure of plant PS I has also been resolved to 4.4 Å resolution (Ben-Shem et al. 2003), which revealed strikingly similar architecture that exclusively retains all the essential features of cyanobacterial counterpart. High-resolution crystallographic structures of the cytochrome (cyt) $b_6f$

complexes from a cyanobacterium and unicellular alga have been respectively determined to 3.0 Å and 3.1 Å resolutions (Kurisu et al. 2003; Stroebel et al. 2003). The structures divulged essentially identical architecture that is organized into functionally active homodimeric form (Fig. 1.2). Furthermore, the crystal structures of cyanobacterial photosystem II (PS II) have been resolved and refined to 3.5 Å resolution (Zouni et al. 2001; Kamiya and Shen 2003; Ferreira et al. 2004). The crystal structure of complete ATP synthase has not yet been determined, however, the medium resolution X-ray structure of ATP synthase containing all major subunits (Stock et al. 1999) and detailed high-resolution structures of various subunits (Rastogi and Girvin 1999; Gibbons et al. 2000) have been resolved.

## 1.4.   Photosynthetic Energy Transduction

Photosystems are constructed around an exquisitely designed basic blueprint. They contain a reaction center (RC) in which the conversion of light energy to electrochemical potential occurs and light-harvesting antenna systems that service the RC so that it can operate efficiently under sunlight, rather dilute source of energy, via collecting light and then delivering the energy. Photosynthesis is initiated by the absorption of a photon in one of the many chlorophyll (Chl) and other pigment molecules associated with light-harvesting antenna systems. The resulting electronic excitation moves from pigment to pigment in the light-harvesting antenna systems, via Förster energy transfer mechanism (Section 3.1). In the course of this random walk, which may be much less random due to specific arrangements of pigments in a funnel-like or downhill-like manner, the excitation will visit the RC that consists of several pigment molecules arranged in two pseudo-$C_2$ symmetrical branches.

Once the excitonic energy reaches the RC, it has high probability to be trapped photochemically in the RC. In particular, a special pair of Chl *a* molecules, spectroscopically identified as the primary electron donor P700 and P680 act as an excitation trap in the PS I and PS II RCs, respectively. Once the special pair is excited as the result of the excitation transfer from the antenna system, its electron donating potential becomes more negative by a value approximately equal to the singlet excited

energy, which is, in the essence, how light energy is converted into electrochemical energy in the RC (wavy arrows in Fig. 1.2). This light-induced reducing potential change enables an electron to be transferred in exothermic (downhill) manner to a pigment molecule, spectroscopically identified as the primary electron acceptor at first and sequentially to other cofactors of the RC vectorially across the thylakoid membrane. This transmembrane electron transfer (ET) processes would be thermodynamically endothermic (uphill) without the input of the absorbed photon energy (Fig. 1.2).
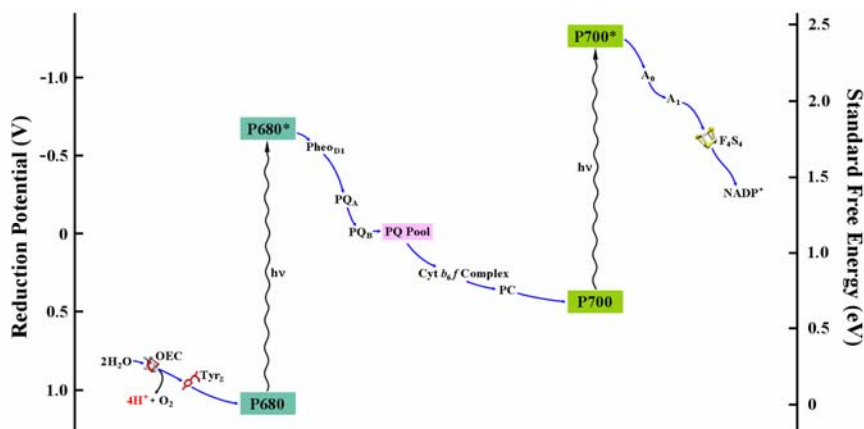


**Fig. 1.2** The Z-scheme of photosynthesis. PS I and PS II cooperatively use the energy of absorbed photons to transport electrons abstracted from $H_2O$ across the thylakoid membrane along a chain of cofactors that are interconnected by highly mobile electron carriers and the cyt $b_6f$ complex, which ultimately reduces $NADP^+$ to NADPH, which is a source of reducing equivalents of many reductive biosynthetic reactions including conversion of atmospheric $CO_2$ to carbohydrates. Approximate standard free energy levels are indicated on the right-scale, in which the standard free energy of P680 is arbitrarily set to zero. Reduction midpoint potentials (vs. NHE) are indicated on the right-scale. The energy of absorbed photons is to drive ET via excitation induced change in reduction potentials of the primary electron donors in the RCs.

In PS II, the electronically excited primary electron donor P680* ejects a light-driven electron and reduces the electron stabilizing acceptor $PQ_A$, a plastoquinone that is tightly bound at the stromal side of PS II via the primary electron acceptor $Pheo_{D1}$ (Fig. 1.2) (Diner and Rappaport 2002; Iwata and Barber 2004). After each of four of this asymmetric ET, $P680^{\bullet+}$ extracts one electron from the oxygen-evolving center (OEC), a cluster of four manganese atoms and one $Ca^{2+}$ ion that bind two substrate water molecules (Ferreira et al. 2004), by means of the redox-active tyrosine residue $Tyr_Z$

(Fig.1.2). In turn, the four positive charges accumulated in the OEC oxidize the two bound $H_2O$ molecules, coupled with the release of $O_2$ and four protons ($H^+$) (Fig. 1.2),

$$2H_2O \xrightarrow{\text{hv}} 4H^+ + 4e^- + O_2 \tag{1.2}$$

Molecular $O_2$ released as a by-product in this light-induced oxidation of water, which is one of the most thermodynamically demanding reactions in biological systems, attributes to oxygen evolvement of photosynthesis. In the first two charge separations, $PQ_A$ doubly reduces pseudo-$C_2$ symmetrically related $PQ_B$, a mobile plastoquinone loosely bound to the $PQ_B$ binding site of PS II (Fig. 1.2). Subsequently, $PQ_B$ uptakes two protons for electroneutrality from the stromal side of thylakoid membrane, forming plastoquinol $PQH_2$ that is released into the plastoquinone pool embedded in the thylakoid membrane matrix (Fig. 1.3). A new PQ from the plastoquinone pool is inserted into the $PQ_B$ binding niche for another round of reduction and release.

Lipophilic plastoquinol $PQH_2$ released into the PQ pool as the result of the light-induced redox reactions of PS II diffuses through the thylakoid membrane matrix and binds to the $Q_p$ site of the integral membrane cyt $b_6f$ complex (Fig. 1.3). Subsequently, the cyt $b_6f$ complex oxidizes the bound $PQH_2$ and reduces plastocyanin (PC) in the stromal aqueous phase (Fig. 1.3), wherein PC is a small copper-binding protein that functions as an electron shuttle from the $b_6f$ complex to the PS I RC (Cramer et al. 2004). This intra-protein ET process within the cyt $b_6f$ complex is coupled to proton translocation across the thylakoid membrane that generates a transmembrane electrochemical proton gradient via the Q-cycle mechanism of the $b_6f$ complex, which will be discussed in the subsequent section in more detail.

The transmembrane electrochemical proton gradient drives protonic flow from the lumen to the stromal side of thylakoid membrane that is allowed only through the transmembrane region of the ATP synthase (Fig. 1.3), which is coupled to rotational motion of the central cylinder and rotor stalk (Junge et al. 1997; Yoshida et al. 2001). The rotation of the rotor stalk induces alternating conformational changes in the three nucleotide-binding sites of the catalytic β subunits, the rotation of which is prevented by the stator stalk (Fig. 1.3). These rotation-induced conformational changes occur in a such way that in one catalytic nucleotide-binding site, which is of very high nucleotide-

binding affinity, adenosine diphosphate (ADP) and inorganic phosphate $P_i$ are abstracted from the stromal phase, in another catalytic site, adenosine triphosphate (ATP) forms reversibly from ADP and $P_i$, due to tight sequestration of products and substrates, and finally in other catalytic nucleotide-binding site, the nucleotide-binding affinity is drastically reduced via changing the structure of the site where numerous protein-to-ATP interactions, e.g., hydrogen-bonds, hydrophobic interactions and salt-bridges, are broken, thus allowing synthesized ATP release into the stroma (Boyer 1997; Senior et al. 2002).
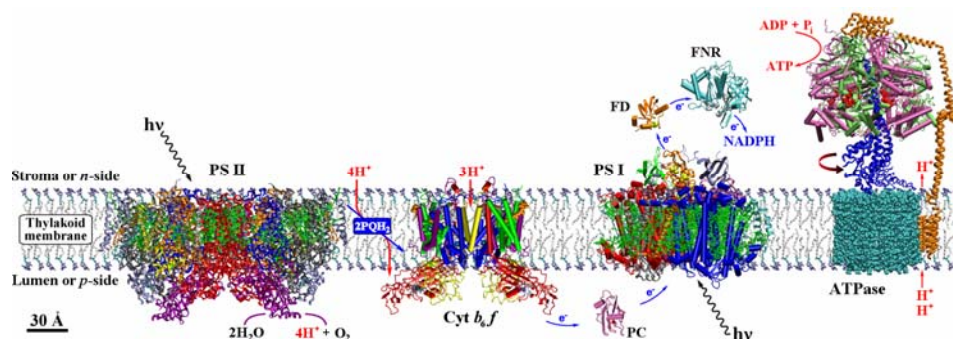


**Fig. 1.3** The photosynthetic energy transducing chain in the context of the crystallographic structures, showing electron and proton transport pathways for one photosynthetic turnover**.** The vectorial electron transport pumps protons ($H^+$) in the opposite direction, into the thylakoid lumen that leads to a transmembrane electrochemical potential gradient of proton concentration, which is utilized by the molecular rotary engine, ATPase to drive the synthesis of ATP, the energy currency of biological systems, from ADP and inorganic phosphate $P_i$. NADPH and ATP are used to reduce $CO_2$ to carbohydrates in the subsequent enzyme-catalyzed dark reactions. PC, FD and FNR models are based on the available high-resolution crystal structures (Karplus et al. 1991; Redinbo et al. 1993; Kurisu et al. 2001).

The primary photochemical reactions in PS I also follow the universal scheme. Excitonic energy transfer from the light-harvesting antenna system results in electronic excitation of the primary electron donor P700, followed by the primary charge separation via ET from the primary donor to the primary electron acceptor $A_0$, a Chl *a* molecule, forming the primary radical pair $P700^{\bullet+}A_0^{\bullet-}$ (Savikhin 2005). The primary charge separation in PS I is stabilized by subsequent ET from $A_0^{\bullet-}$ to $A_1$, a phylloquinone molecule, and then sequentially to the terminal electron acceptors $F_X$, $F_A$ and $F_B$, $F_4S_4$ clusters. In turn, the reduced terminal acceptor donates its excess electron to Ferredoxin-$NADP^+$ oxidoreductase (FNR) via water soluble ferredoxin (FD), a redox-active protein

containing $Fe_2S_2$ cluster on the stromal of the thylakoid membrane, while the oxidant $P700^{\bullet+}$ abstracts an electron from the redox-active mobile electron carrier PC reduced as the result of the intra-protein ET in the cyt $b_6f$ complex on the lumen side (Chitnis 2001). Thereby, PS I uses the energy of absorbed photons to translocate electrons across the thylakoid membrane to FNR that uses the transported electrons shuttled from PS I, one at a time, by mobile electron carrier FD and protons from aqueous stromal phase to convert oxidized form of nicotinamide adenine dinucleotide phosphate $NADP^+$ into its reduced form NADPH (Fig. 1.3).

The principal products, ATP and NADPH, generated in the light-driven reactions are energy-rich compounds of intermediate stability, as they are not suitable for long-term storage of energy. Thus, in the subsequent series of enzyme-catalyzed reactions, ATP and NADPH are used in the fixation of carbon dioxide ($CO_2$) to carbohydrates such as sucrose and starch that are more stable form suitable for long-term storage of energy, such as building plant biomass, through the metabolic pathway known as the Calvin-Benson-Bassham (CBB) cycle (Calvin 1992), completing a cycle of photosynthesis.

## 1.5. Cytochrome $b_6f$ Complex: Plastoquinol-Plastocyanin Oxidoreductase

As we have briefly discussed in the preceding section, the multisubunit cyt $b_6f$ integral membrane protein complex mediates ET between the RCs of PS II and PS I by oxidizing lipophilic plastoquinol and reducing plastocyanin (Cramer et al. 1996). Consistent with a basic paradigm of membrane-based energy transduction (Mitchell 1975), ET through the cyt $b_6f$ complex is coupled to vectorial proton translocation across the thylakoid membrane (Cramer 2004).

High-resolution crystallographic structures of the cyt $b_6f$ complexes from the thermophilic cyanobacterium *M. laminosus* (Kurisu et al. 2003) and the unicellular green alga *C. reinhardtii* (Stroebel et al. 2003) have been determined. The crystal structures divulged essentially identical architecture, which in itself is astounding given that the two organisms are evolutionarily separated by $10^9$ years (Cramer et al. 2004). Dimensionally, the cyt $b_6f$ complex extends 100 Å along the thylakoid membrane normal, and has

dimensions of 90×55 Å within the thylakoid membrane on the stromal side, and of 120×75 Å extrinsic to the membrane on the lumen side (Kurisu et al. 2003).

The cyt $b_6f$ complex (molecular weight of 217 kD) is organized into homodimeric form which has been revealed to be the functionally active form of the complex (Huang et al. 1994). According to the crystal structures (Kurisu et al. 2003; Stroebel et al. 2003), the monomeric unit of the cyt $b_6f$ complex consists of four large subunits, cyt $f$, cyt $b_6$, the Rieske iron-sulfur protein (ISP), subunit IV, and four small subunits, PetG, PetL, PetM, and PetN (Fig. 1.4). In addition, the $b_6f$ monomer contains seven natural prosthetic groups: four hemes, one $Fe_2S_2$ cluster, one Chl $a$ and one β-carotene.
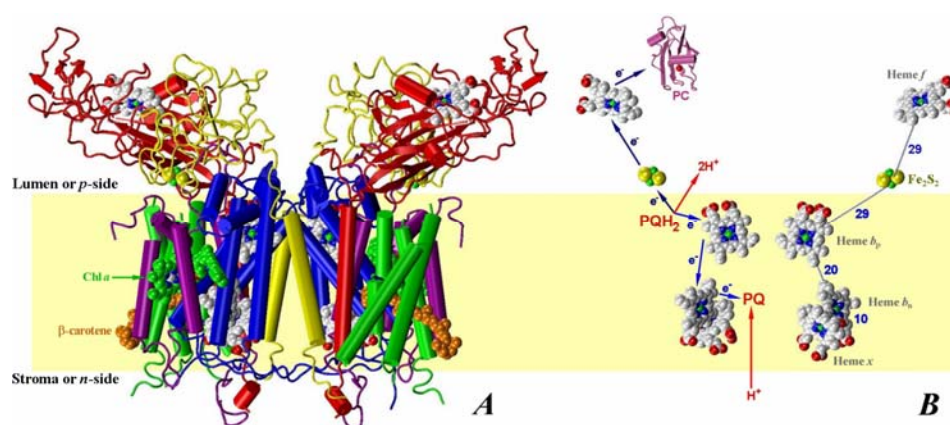


**Fig. 1.4** The eight subunit dimeric cyt $b_6f$ complex of the thermophilic cyanobacterium *M. laminosus* (Kurisu et al. 2003). (A) Side view showing bound cofactors and protein subunits. The color code is as follows: cyt $b_6$ (blue); subunit IV (purple); cyt $f$ (red); ISP (yellow); PetG, PetL, PetM and PetN (green); and hydrophobic part of the thylakoid membrane (yellow band). (B) Electron and proton transfer pathways through the cyt $b_6f$ complex, showing electron and proton stoichiometry for one turnover of the complex, and center-to-center distances between redox cofactors.

The two monomers are related by a $C_2$ axis perpendicular to the thylakoid membrane plane, and surround a large protein-free central cavity known as a quinone exchange cavity. The ISP contributes to dimer stability by domain swapping: Its transmembrane helix obliquely spans the thylakoid membrane in one monomer, and its extrinsic domain is part of the other monomer (Kurisu et al. 2003) (Fig. 1. 4A).

Lipophilic plastoquinol $PQH_2$ released into the PQ pool as the result of the light-induced redox reactions of PS II diffuses through the thylakoid membrane matrix and

binds to the $Q_p$ binding pocket, a small portal with dimensions of 11×12 Å leading from the quinone exchange cavity bounded by the $Fe_2S_2$ cluster, heme $b_p$ and the loop connecting helices E and F of subunit IV. Within the cyt $b_6f$ complex, one electron from $PQH_2$ is transferred through a high-potential ET chain that consists of the ISP and cyt $f$. This results in the release of two protons to the aqueous lumenal phase of the thylakoid membrane (Fig. 1.4B). The second electron from $PQH_2$ is transferred across the complex through two $b$ hemes (Trumpower 1990; Kramer and Crofts 1993; Berry et al. 2000), or as anionic plastosemiquinone (Girvin and Cramer 1984; Joliot and Joliot 1994), and the resulting proton uptake from the stromal side contributes to the electrochemical proton gradient across the thylakoid membrane (Fig. 1.4B).

### 1.5.1.    A Mystery of the Unique Chl $a$ Molecule

The crystal structures of the cyt $b_6f$ complex confirmed the presence of the single Chl $a$ molecule as an intrinsic component of the complex (Kurisu et al. 2003; Stroebel et al. 2003). The role of this Chl $a$ remains a mystery (Kühlbrandt 2003)—the cyt $b_6f$ complex does not participate in light harvesting nor does it utilize the Chl $a$ in its ET chain. However, independent of its functional role, a Chl $a$ molecule is known to produce highly toxic singlet oxygen as the result of energy transfer from its excited triplet state to oxygen molecule (Fujimori and Livingston 1957). Therefore, it endows with paradoxical problem that we will address in Chapter 4 on the basis of our recently published manuscripts (Dashdorj et al. 2005c; Dashdorj et al. 2005d).

### 1.6.    Photosystem I: Plastocyanin-Ferredoxin Oxidoreductase

As concisely discussed in Section 1.4, PS I acts in series with PS II as a driving force, utilizing the energy of absorbed photons, in linear electron transport from $H_2O$ to $NADP^+$ vectorially across the thylakoid membrane along a chain of cofactors that are interconnected by highly mobile electron carriers and the cyt $b_6f$ complex, generating NADPH, a source of reducing equivalents of many reductive biosynthetic reactions including conversion of atmospheric $CO_2$ to carbohydrates (Chitnis 2001).

According to the crystal structure of PS I from the thermophilic cyanobacterium *S. elongatus* at 2.5 Å resolution (Jordan et al. 2001), monomeric PS I contains 12 protein subunits and 127 cofactors consist of 96 Chl *a* molecules, 2 phylloquinones, 3 $Fe_4S_4$ clusters, 22 β-carotenes, 4 lipids, one putative $Ca^{2+}$ ion and 201 water molecules, leading to molecular weight of 356 kD (Fig. 1.5). The large polypeptide subunits PsaA and PsaB bind most of the cofactors and related by a pseudo-$C_2$ axis.



**Fig. 1.5** Side view of the twelve subunit monomeric PS I core complex of the thermophilic cyanobacterium *S. elongatus* (Jordan et al. 2001). The color code of subunits visible in the figure is as follows: PsaA (blue); PsaB (red); PsaC (orange); PsaD (light blue); PsaE (light green); PsaF (silver); PsaJ (helical orange); PsaK (cyan); and Chl *a* molecules (green). Iron and sulfur atoms of the three $Fe_4S_4$ clusters presented as white and yellow space filling spheres, respectively. Pathway of ET extrinsic to PS I that drives the reduction of $NADP^+$ to NADPH is explicitly illustrated.
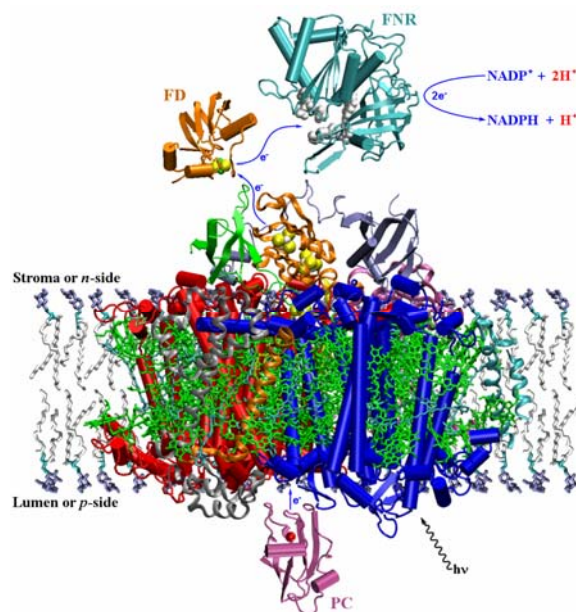
PS I contains extensive internal light-harvesting antenna system that is formed by 90 Chl *a* molecules and 22 β-carotenes (Fig. 1.6). The antenna pigments are arranged in quasi-elliptical manner around the RC as highlighted in Fig. 1.6B. Within the antenna system, the average distance from any of the pigments to its nearest neighbor is 9.9 Å, which is favorable range for rapid excitation energy transfer, which transpires via the Förster mechanism. Calculation based on the Förster energy transfer theory predicts that single energy transfer step in antenna occurs within 100–200 fs (Section 3.1). Therefore, excitation energy is rapidly equilibrated between antenna pigments, which in turn ensures extremely efficient excitation energy transfer to the PS I RC. Indeed, the overall lifetime of electronic excitation has been shown to be rather short (Savikhin 2005). For instance: effective trapping time of ~24 ps was measured for PS I complex from *Synechocystis* sp. PCC6803 (Hastings et al. 1994; Savikhin et al. 2000).
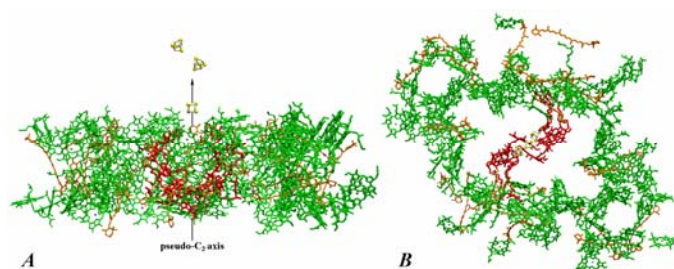
**Fig. 1.6** Spatial organization of the cofactors of the RC and the intrinsic antenna system of PS I (Jordan et al. 2001). The RC cofactors are shown in red sticks, while Chl *a* molecules and β-carotenes associated with antenna depicted in green and orange sticks correspondingly. Fe and S atoms in the $Fe_4S_4$ clusters are respectively presented in white and yellow spheres. (A) Side view. (B) View from stromal side onto the thylakoid membrane plane.

The functionally most important part of PS I is the RC that consists of three pairs of Chl *a* molecules and a pair of phylloquinones that are coordinated by the PsaA and PsaB polypeptides: a Chl *a/a′* heterodimer spectroscopically identified as the electron donor P700, two Chl *a* molecules identified as $A_{-1}$, two Chl *a* molecules identified as $A_0$, and two phylloquinones identified as $A_1$. These cofactors are arranged into two symmetric branches related by pseudo-$C_2$ axis that diverge at P700 and converge at the iron-sulfur cluster $F_X$.

**Fig. 1.7** The ET cofactors of PS I from the thermophilic cyanobacterium *S. elongatus* (Jordan et al. 2001). The cofactors are arranged into two symmetric branches of PsaA and PsaB related by an internal twofold axis. The crystallographic nomenclature for the cofactors is depicted next to the cofactor, and the spectroscopic nomenclature for the cofactors is depicted in the center. The center-to-center distances (in Å) between the cofactors are explicitly indicated.
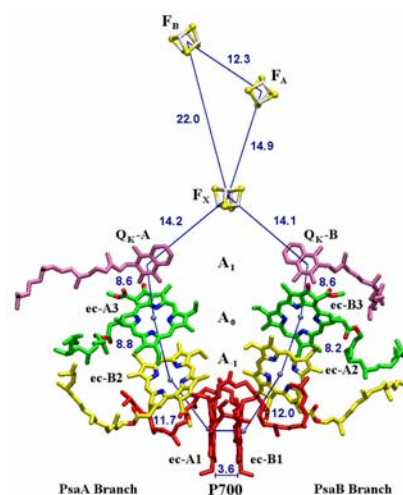


After the creation of P700* as the result of the excitonic energy transfer from the light-harvesting antenna system, the excitation energy is photochemically trapped in the primary charge separation via the formation of the primary radical pair $P700^{\bullet+}A_0^{\bullet-}$, which is generally accepted to occur within the 1–3 ps intrinsic lifetime range (Brettel 1997; Savikhin 2005). The electron localized on the primary electron acceptor $A_0$ is then transferred to the secondary electron acceptor $A_1$ within 10–50 ps  (Brettel and Leibl

2001; Savikhin 2005). Subsequently, the unpaired electron migrates from $A_1$ to the $Fe_4S_4$ center $F_X$ and finally to the terminal iron-sulfur clusters $F_A$ and $F_B$ all occurring with kinetics in nanosecond time domain before being transferred to soluble FD, which diffuses through the stromal aqueous phase and donates the electron to FNR (Fig. 1.5).

## 1.6.1. Directionality of Electron Transfer: Symmetry or Asymmetry?

The presence of two highly symmetrical branches of cofactors in the PS I RC raises the intriguing question of whether one or both are active in ET. To resolve this issue, we applied optical femtosecond pump-probe techniques to study the ET dynamics in two complimentary pairs of point mutants in both the PsaA and PsaB branches of cyanobacterial PS I. The experimental data and analysis revealed that transmembrane ET in cyanobacterial PS I is asymmetric and occurs primarily along the PsaA branch of cofactors. We have recently published a manuscript describing these results (Dashdorj et al. 2005b; Dashdorj et al. 2005a), which will be discussed in Chapter 5 in more detail.

## 1.6.2. Electron Transfer Induced Stark Effect

There is general agreement that the reduction of $A_1$ is complete within a few tens of picoseconds at most and the Chl $a$ $Q_y$ spectral evolution that stems from all of the preceding processes are complete within this time. While the consequent ETs from $A_1$ to iron sulfur clusters do not affect the Chl $a$ population directly, the presence of a strong local electric field around these ET cofactors must affect the optical properties of the nearby pigments (Steffen et al. 1994). It had been reported that noticeable optical absorption evolution in the Chl $a$ $Q_y$ spectral region spans well into the nanosecond range (Savikhin et al. 2001). We have performed detailed analysis of this effect and proposed that the shape and the magnitude of these changes are more consistent with electrochromic shift of Chl $a$ absorption bands which accompanies ET from $A_1$ to $F_X$. Based on the measured data, we estimated the effective dielectric constant deep within PS I and reveal that significant local reorganization of the interior of the protein occurs, leading to effective charge screening. These findings were recently published as a manuscript (Dashdorj et al. 2004), and will be discussed in more detail in Chapter 6.

CHAPTER 2. EXPERIMENTAL METHODS

In this chapter, we briefly review pump-probe absorption difference spectroscopy used for the study of energy and electron transfer processes within photosynthetic systems. Moreover, concise description of the state-of-the-art ultrafast time-resolved pump-probe system used throughout out this work is given.

2.1. Pump-Probe Absorption Difference Spectroscopy

In a typical pump-probe absorption difference experiment, a laser pulse generally referred as pump is used to excite a molecule in a sample of interest. As the molecule is promoted into its excited state, the absorption spectrum of the sample changes, reflecting the optical properties of the excited molecule. The resulting difference between the absorption spectra before and after the excitation ($\Delta A$) is then probed as a function of time and wavelength by another laser pulse generally referred as probe, thus attributing the name of pump-probe absorption difference spectroscopy.

There are three major contributions to the absorption difference signal $\Delta A$ when a molecule is excited: photobleaching (PB) of the original absorption spectrum of the excited molecule, excited state absorption (ESA) that arises as a result of the transitions from the excited state to the higher excited states, and stimulated emission (SE) due to the stimulated transition from the excited state to the ground state of the excited molecule. These three components of the $\Delta A$ signal are superimposed and, in general, cannot be measured independently in a pump-probe experiment.

The time resolution of a pump-probe apparatus is typically limited by the duration of the laser pulse and can be better than 100 fs. The sensitivity of the $\Delta A$ signal to both the

ground and excited state populations allows not only detection of excitation energy transfer dynamics, but also ET kinetics which involves optically visible cofactors. Furthermore, when the excitation energy is transferred between spectrally distinct molecules, the dynamics of this process is reflected in the $\Delta A$ signal.

## 2.2. Overview of Femtosecond Time-Resolved Pump-Probe System

Overall schematic of our home-built state-of-the-art femtosecond time-resolved pump-probe system is shown in Fig. 2.1. More detailed schematic and description of individual components are provided in Appendix I.
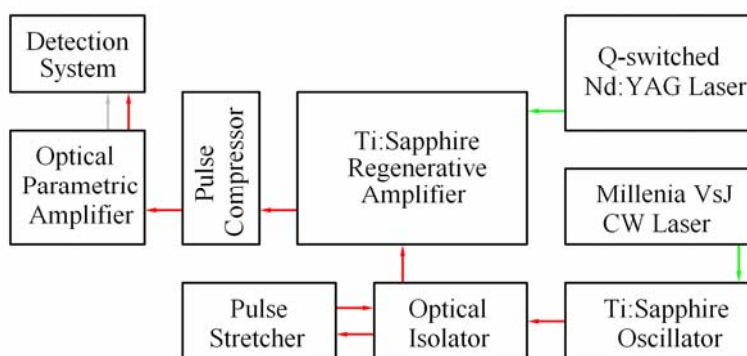


**Fig. 2.1** Overview schematic of the femtosecond time-resolved pump-probe system. Arrows represent the paths of laser beams. Wavelength of laser beams is approximated in color. The system has time resolution of 100 fs and wavelength tunability covering the entire range from the visible to the infrared.

The self-mode-locked Ti:sapphire (T:S) oscillator pumped generated a pulse train of ~70 fs duration pulses around 780 nm spaced at the cavity round trip time of ~12 ns (Fig A.1). In order to investigate ultrafast dynamics in photosynthetic complexes, one needs broad wavelength tuning range covering the visible spectrum (400–800 nm). Although, self-mode-locked T:S laser provides the time resolution (~70 fs) to study ultrafast dynamics, its wavelength tunability is rather limited (680–900 nm). One of the attractive choices is to utilize nonlinear optical processes to generate broad tunability, in which high pulse energy is requisite. Thus we amplify the output of the T:S oscillator in a T:S regenerative amplifier (Fig. A.2). High peak power pulses have a tendency to self-focus in condensed media, which may cause damage to the optics. To prevent that, the pulses

were deliberately chirped increasing the pulse duration and reducing the peak power in a pulse stretcher (Fig. A.1). Since we have design that has amplified pulse following the reverse path, high quality isolation is necessary as even a very weak reflection that gets back into the T:S oscillator can disrupt the modelocking. Isolation is achieved by using an optical isolator (Fig. A.1), which acts as a one-way valve for linearly polarized light. After amplification, the pulses are recompressed back to short duration via removing the chirp in a pulse compressor (Fig. A.2). The resulting high energy short duration pulses converted in an optical parametric amplifier (OPA) into infrared signal and idler frequencies in order to have two independently tunable pulse sources, each capable of accessing a very broad wavelength, while maintaining the short pulse duration (Fig. A.3).

In pump-probe experiments, the second-harmonic of OPA signal pulses served as pump, while the broadband continuum pulses generated in a sapphire crystal are used as probe to detect the pump-induced change in absorbance of the sample ($\Delta A$). The absorbance change is measured as a function of both the probe wavelength and the time delay between the pump and probe pulses in ultra sensitive detection system that has shot noise-limited noise performance (Fig. A.3).

CHAPTER 3.  THEORETICAL METHODS

In this chapter, we briefly review theoretical mechanisms for electronic excitation and ET among photosynthetic pigments that recur throughout this proposal.

3.1.   Theory of Excitonic Interaction and Electronic Energy Transfer

Electronic energy transfer processes occur via an intermolecular Coulombic interaction $V_{DA}$ between the excitation energy donating molecule, the donor, D, and the excitation energy accepting molecule, the acceptor, A (van Grondelle et al. 1994; Struve 1995). The rate of energy transfer $k_{DA}$ is governed by matrix element $U_{DA}$, which has two contributions. The first contribution is generally called the Coulombic term ($U_{DA}^{c}$), in which the initially excited electron on D returns to the ground state, while simultaneously an electron on the ground state orbital of A is excited (Fig. 3.1). The second term is called the electron exchange term ($U_{DA}^{ex}$), in which the energy transfer process is coupled to an exchange of two electrons on D and A (Fig. 3.1).

**Fig. 3.1** Schematic representation of the Coulombic (left) and the exchange contribution (right) to electronic excitation energy transfer.
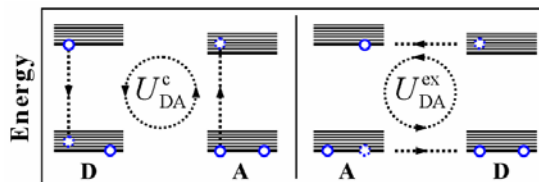


The exchange energy transfer mechanism is only operative when the wave functions overlap significantly, meaning that distances between the molecules should almost be within the van der Waals contact. In contrast to that, the Coulombic mechanism is effective over large distances. The exchange mechanism is dominant if the energy

transfer involves optically forbidden states on the molecules, as is in the case of triplet energy transfer (van Grondelle 1985).

If the Coulombic term $U_{DA}^c$ is much larger than the width of the individual transitions involved (A→A* or D→D*), the coupling is strong (strong coupling limit), and the excitation is delocalized over D and A. The combined spectrum of D and A is modified due to transitions of the in-phase and out-of-phase combination of the locally excited states (excitonic states). In the strong coupling limit the transfer of excitation is a coherent process. The excitation shuttles between D and A and is never more than instantaneously localized on either molecule (van Grondelle 1985). An example of strongly coupled molecules is P700 in the PS I RC, which is heterodimeric pair of Chl *a*/*a′* molecules with the chlorin planes are parallel at 3.6 Å interplanar distance (Fig. 1.7).

If the interaction energy $U_{DA}$ is smaller than the width, the coupling is weak (the weak coupling limit), and the classical electrostatic intermolecular interaction energy has the following from (Struve 1995),

$$V_{DA} = \sum_{\substack{i \in D \\ j \in A}} \frac{q_i\, q_j}{r_{ij}} \tag{3.1}$$

where $r_{ij}$ is the separation between charges $q_i$ and $q_j$, and the indices $i, j$ indicate charges on molecules D and A, respectively. If the intermolecular separation $R$ is large compared to the molecular size, so that the overlap between the respective electronic charge distributions is small, it is useful to expand the interaction energy $V_{DA}$ in a power series (Hirschfelder and Meath 1967),

$$V_{DA} = \sum_{n=1}^{\infty} \frac{V_n}{R_n} \tag{3.2}$$

After substitution of explicit expressions for the coefficients in this multipole expansion, the electrostatic interaction energy assumes the following form in terms of the electric charges and the transition dipole moments $\vec{\mu}_D$ and $\vec{\mu}_A$ (Struve 1995),

$$V_{DA} = \frac{q_D q_A}{R} + \frac{q_D\left(\vec{\mu}_A \cdot \vec{R}\right) - q_A\left(\vec{\mu}_D \cdot \vec{R}\right)}{R^2} + \frac{\vec{\mu}_D \cdot \vec{\mu}_A - 3\left(\vec{\mu}_D \cdot \vec{R}\right)\left(\vec{\mu}_A \cdot \vec{R}\right)}{R^3} + \ldots \tag{3.3}$$

Here the vector $\vec{R}$ points from the center of D to the center of A. The successive terms in Eq. 3.4 represent the charge-charge, charge-dipole and dipole-dipole contributions to the total electrostatic energy. In the case where both molecules are uncharged, the terms involving charges drop out, and the lowest order nonvanishing term in the multipole expansion corresponds to the dipole-dipole interaction,

$$V_{DA} \approx \frac{\vec{\mu}_D \cdot \vec{\mu}_A - 3(\vec{\mu}_D \cdot \vec{R})(\vec{\mu}_A \cdot \vec{R})}{R^3} \tag{3.5}$$

Using Fermi's Golden Rule, the rate of energy transfer from D* to A can be calculated in the limit of weak intermolecular coupling (Gottfried and Yan 2004),

$$k_{DA} = \frac{2\pi}{\hbar} \left| \left\langle \Psi(D^*A) \middle| V_{DA} \middle| \Psi(DA^*) \right\rangle \right|^2 \rho(E) \tag{3.6}$$

where $\rho(E)$ is the density of states isoenergetic with the initial level in the final manifold states. If the total energies of D and A in their ground state are $\varepsilon_D$ and $\varepsilon_A$; the corresponding energies for the excited states are $\varepsilon_D^*$ and $\varepsilon_A^*$, then integration over all allowed combinations of initial and final D and A energies yields

$$k_{DA} = \frac{2\pi}{\hbar} \frac{1}{g_D^* g_A} \int dE \int p_A(\varepsilon_A) d\varepsilon_A \int p_D^*(\varepsilon_D^*) \left| \left\langle \Psi(D^*A) \middle| V_{DA} \middle| \Psi(DA^*) \right\rangle \right|^2 d\varepsilon_D^* \tag{3.7}$$

where $p_D^*$ and $p_A$ denote the initial energy distributions on D and A; $g_D^*$ and $g_A$ are the state degeneracies of D* and A; and $E = \varepsilon_D^* - \varepsilon_D = \varepsilon_A^* - \varepsilon_A$. According to Eq. 3.5, the leading term in the matrix element required to evaluate the rate for energy transfer between uncharged D and A molecules becomes

$$\left| \left\langle \Psi(D^*A) \middle| V_{DA} \middle| \Psi(DA^*) \right\rangle \right|^2 = \frac{\kappa^2}{R^6} \left| \left\langle \Psi(D^*) \middle| \mu_D \middle| \Psi(D) \right\rangle \right|^2 \left| \left\langle \Psi(A) \middle| \mu_A \middle| \Psi(A^*) \right\rangle \right|^2 \tag{3.8}$$

where $\kappa^2$, the dipole-dipole orientational factor that can evidently assume values from 0 to 4 as we respectively define angles $\alpha$, $\beta_1$ and $\beta_2$ between the unit vectors, is given by

$$\kappa^2 = \left( \hat{\mu}_D \cdot \hat{\mu}_A - 3(\hat{\mu}_D \cdot \hat{R})(\hat{\mu}_A \cdot \hat{R}) \right)^2 = \left( \cos\alpha - 3\cos\beta_1 \cos\beta_2 \right)^2 \tag{3.9}$$

It can be shown (Birks 1970) that the rate for spontaneous electric dipole emission of a photon with energy $E$ by excited donor D* is

$$\frac{1}{\tau_D} = \frac{4E^3 n^3}{3\hbar^4 c^3 g_D^*} \int p_D^*\left(\varepsilon_D^*\right) \left|\left\langle \Psi\left(D^*\right) \right| \mu_D \left| \Psi\left(D\right) \right\rangle\right|^2 d\varepsilon_D^* \tag{3.10}$$

it follows that

$$\int p_D^*\left(\varepsilon_D^*\right) \left|\left\langle \Psi\left(D^*\right) \right| \mu_D \left| \Psi\left(D\right) \right\rangle\right|^2 d\varepsilon_D^* = \frac{3\hbar^4 c^3 g_D^*}{4E^3 n^3 \tau_D} f_D(E) \tag{3.11}$$

where $f_D(E)$ is the donor emission spectrum normalized to unity. The Einstein coefficient, which relates to the molecular absorption cross-section $\sigma_A(E)$ (Birks 1970), for dipole absorption of a photon with energy $E$ by the acceptor molecule A is

$$B_A(E) = \frac{2\pi}{3\hbar^2 g_A} \int p_A\left(\varepsilon_A\right) \left|\left\langle \Psi\left(A\right) \right| \mu_A \left| \Psi\left(A^*\right) \right\rangle\right|^2 d\varepsilon_A = \frac{c}{3n\hbar^3 g_A E} \sigma_A(E) \tag{3.12}$$

Substituting Eq. 3.11 and Eq. 3.12 into Eq. 3.7 with the help of Eq. 3.8, results in the following equation known as the Förster equation (Förster 1948; Förster 1965)

$$k_{DA} = \frac{9c^4}{8\pi n^4} \frac{\kappa^2}{\tau_D R^6} \int f_D(\omega) \sigma_A(\omega) \frac{d\omega}{\omega^4} \equiv \frac{\kappa^2}{\tau_D} \left(\frac{R_0}{R}\right)^6 \tag{3.13}$$

where $\omega$ denotes the circular frequency $E = \hbar\omega$; $R_0$ is the Förster radius that is defined as the distance for which the probabilities for resonance energy transfer and fluorescence are equal; and $\tau_D$ is the radiative fluorescence lifetime of a noninteracting donor molecule, the lifetime the excited state of D would have if only decay via fluorescence were possible, thus differs from the fluorescence lifetime measured in the experiment by the fluorescence quantum yield $\varphi_D$, i.e., $\tau_F = \tau_D \varphi_D$.

The fluorescence lifetime and quantum yield of Chl $a$ have reported to be ~5.5 ns and ~0.32, respectively (Seely and Connolly 1986), which results in the radiative fluorescence lifetime of ~17.2 ns. In addition, for isoenergetic Chl $a$ molecules the Förster radius is found to be ~75 Å (Colbow 1973; van Grondelle 1985). Therefore, the Förster energy transfer rate between two Chl $a$ molecules separated at average distance of 9.9 Å in the PS I antenna system (see Section 1.6) can be estimated with an average orientational value of $\kappa^2 = 0.667$ in the first approximation using Eq. 3.13, which yields ~140 fs. Although, experimentally resolving individual energy transfer step in the PS I antenna system is improbable due to spectral congestion, many single-step energy

transfers have been reported to occur within this time range, for instance, in antenna complex from the green sulfur bacterium (Savikhin et al. 1994).

Since the electric dipole operators $\mu_D$ and $\mu_A$ in Eq. 3.8, do not operate on the electron spin functions, electronic spin is conserved in the Förster energy transfer, and because of the electronic ground states of photosynthetic pigments that are closed-shell singlet states, the Förster energy transfer is thus singlet-singlet process.

## 3.2.  Theory of Electron Transfer

Non-adiabatic ET theory is often applied to elucidate range of ET processes that take place within biological systems (Marcus and Sutin 1985). Intraprotein ET generally takes place via a tunneling mechanism over distances that are relatively large on an atomic scale. Thus, the interaction between the electron donor and acceptor redox centers is typically rather small. Under these conditions Fermi's Golden Rule provides a good first-order description of the rate of non-adiabatic ET (Bolton et al. 1991),

$$k_{ET} = \frac{2\pi}{\hbar} V^2 FC \qquad (3.14)$$

where the electronic coupling matrix element $V^2$ that is critically dependent on the extent of the overlap of the reactant and product electronic wavefunctions, while the Franck-Condon factor $FC$ reflects the integrated overlap of the reactant and product nuclear wavefunctions. Simple approximation based on the tunneling between two narrow potential wells representing the redox centers separated at distance $R$ through a barrier of constant height yields an exponential decay of the electronic coupling (Hopfield 1974),

$$V^2(R) = V_0^2 \exp(-\beta R) \qquad (3.15)$$

The exponential coefficient $\beta$ is essentially a description of how well the electronic wavefunctions penetrate the intervening medium between the redox centers, which is known to be significantly modulated by the medium.

In both classical (Marcus and Sutin 1985) and quantum (Hopfield 1974; Jortner 1976) versions of Marcus ET theory, Franck-Condon factors have been described in a model that approximates reactant and product nuclear wavefunctions as harmonic oscillations

with identical frequencies but with different nuclear positions and free energies. In this description, the Franck-Condon factor is (Bolton et al. 1991),

$$FC = \frac{1}{\sqrt{4\pi\lambda RT}} \exp\left(-\frac{\left(\Delta G^0 + \lambda\right)^2}{4\lambda RT}\right) \tag{3.16}$$

where is $\Delta G^0$ the standard free energy or the free energy difference between the reactant and product potential wells for the ET at a fixed donor-acceptor separation distance $R$ and $\lambda$ is a reorganization energy which contains both protein and vibrational contributions that is, in the essence, the free energy associated with rearranging the equilibrium nuclear configuration of the reactants to that of the products without ET (Fig. 3.2).



**Fig. 3.2** Intersecting parabolic potential energy surfaces of classical reactant and product harmonic oscillators for ET process. The optimum ET rate for a given electronic coupling $V^2$ occurs when the reorganization energy $\lambda$ is equal to $-\Delta G^0$.
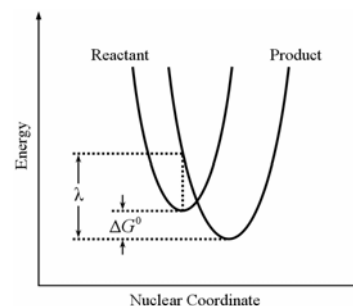
The Marcus relation in Eq. 3.16 predicts that the rate will increase as the standard free energy $(-\Delta G^0)$, and as the standard free energy is increased beyond the reorganization energy, the overlap of the harmonic oscillator nuclear wavefunctions decreases and the rate is expected to fall. This behavior of overall Gaussian dependence of ET rate on the standard free energy defines the Marcus inverted region and has been experimentally verified (Miller et al. 1984).

Based on Marcus ET theory and experimentally observed rates, Dutton and coworkers developed the following semi-empirical relationship for intraprotein ET (Moser et al. 1992; Page et al. 1999),

$$\log k_{ET} = 13 - 0.6\left(R - 3.6\right) - 3.1\left(\Delta G^0 + \lambda\right)^2 \Big/ \lambda \tag{3.17}$$

In this approximation, protein environment is treated as structurally homogenous, which is still a matter of debate (Gray and Winkler 2003). Nevertheless, it appears that most biological ETs occur near the optimum region, thus the rate is primarily determined by the distance between donor and acceptor molecules (Page et al. 1999).

## CHAPTER 4.  THE UNIQUE CHLOROPHYLL MOLECULE

High-resolution crystal structures (Kurisu et al. 2003; Stroebel et al. 2003) of the cyt $b_6f$ complex unambiguously show that a Chl $a$ molecule is an intrinsic component of the $b_6f$ complex. While the functional role of this Chl $a$ remains a mystery (Kühlbrandt 2003), an excited Chl $a$ molecule is known to produce toxic singlet oxygen as the result of energy transfer from the excited triplet state of the Chl $a$ to oxygen molecules. To prevent singlet oxygen formation in light-harvesting complexes, a carotenoid is typically positioned within ~4 Å of the Chl $a$ molecule, effectively quenching the triplet excited state of the Chl $a$. However, in the cyt $b_6f$ complex the β-carotene is too far (14 Å) from the Chl $a$ for effective quenching of the Chl $a$ triplet excited state. In this study, we propose that in this complex, the protection is at least partly realized through special arrangement of the local protein structure that shortens the singlet excited state lifetime of the Chl $a$ by a factor of 20–25 and thus significantly reduces the formation of the Chl $a$ triplet state. Based on optical ultrafast absorption difference experiments and structure-based calculations, we inferred that the Chl $a$ singlet excited state lifetime is shortened due to electron exchange transfer with the nearby tyrosine residue. This kind of protection mechanism against singlet oxygen has not yet been reported for any other Chl-containing protein complex. We also report that the Chl $a$ molecule in the cyt $b_6f$ complex does not change orientation in its excited state.

This chapter is based on the following manuscripts:

Dashdorj N., H. Zhang, H. Kim, J. Yan, W.A. Cramer and S. Savikhin. 2005. The single chlorophyll a molecule in the cytochrome $b_6f$ complex: Unusual optical properties protect the complex against singlet oxygen. *Biophys. J.*: 88:1-10.

Dashdorj N., H. Zhang, H. Kim, J. Yan, W.A. Cramer and S. Savikhin. 2005. Unusual optical properties of the monomeric chlorophyll $a$ in the cytochrome $b_6f$ complex of oxygenic photosynthesis. *In* Photosynthesis: Fundamental Aspects to Global Perspectives. A. van der Est and Bruce D., Editors, ACG Publishing, Lawrence, KS, U.S.A. 451-453.

### 4.1. On the Presence of the Single Chl *a* Molecule

The crystal structures unequivocally confirm the earlier findings through biochemical analysis (Huang et al. 1994; Pierre et al. 1995) of a Chl *a* molecule as an intrinsic component of the cyt $b_6f$ complex and raises intriguing questions about the role of the Chl *a*. The function of the cyt $b_6f$ complex does not require light-harvesting, and the Chl *a* molecule is not part of the ET chain, which are the usual functions of Chl molecule in photosynthetic complexes. Moreover, the functionally similar cyt $bc_1$ complex of the respiratory chain does not contain a Chl *a* molecule (Xia et al. 1997; Iwata et al. 1998).

Regardless of the role of the Chl *a* in the cyt $b_6f$ complex, the introduction of the Chl molecule into the structure may pose a serious threat to the stability of the complex. The triplet excited state of Chl *a* molecule ($^3$Chl*) is known to transfer its energy with high efficiency to oxygen, generating singlet oxygen ($O_2$*) that is extremely toxic to the pigment-protein complex (Fujimori and Livingston 1957; Krinsky 1979). Under illumination, the triplet excited state of monomeric Chl *a* in solution forms with high quantum yield (~64%) through intersystem crossing from the Chl *a* singlet excited state (Chl*) (Bowers and Porter 1967). To prevent singlet oxygen formation in Chl-containing proteins, carotenoid (Car) is typically positioned close (~4 Å) to the Chl *a* molecule, effectively quenching the triplet excited state of the Chl *a* due to rapid triplet-triplet energy transfer to Car (Foote 1976; Siefermann-Harms 1987). It was widely expected that a similar protection mechanism would exist in the $b_6f$ complex. In fact, along with the Chl *a*, a β-carotene was found to be stoichiometrically bound in the $b_6f$ complex (Zhang et al. 1999). It was also reported that, qualitatively, the Chl *a* photodegradation rate depended inversely on the Car concentration (Zhang et al. 1999).

However, the structures of the cyt $b_6f$ complex (Kurisu et al. 2003; Stroebel et al. 2003) show that the β-carotene is too far removed from the Chl *a* for effective direct quenching of the Chl *a* triplet excited state (Fig. 4.1). Triplet-triplet energy transfer from $^3$Chl* to Car occurs via Dexter exchange mechanism and requires the interacting cofactors to form a collision complex, restricting triplet-triplet energy transfer to rather short distances (Renger 1992; van Grondelle et al. 1994).

In this study, we report that effective protection against singlet oxygen formation in the cyt $b_6f$ complex is, at least in part, realized through an alternative mechanism that has not been reported previously. Optical ultrafast pump-probe experiments reveal that the Chl $a$ in the enzymatically active and ultrapure cyt $b_6f$ complex exhibits an unusually short excited state lifetime of ~200 ps that is a factor of ~25 times shorter than the fluorescence lifetime of monomeric Chl $a$ in solution. We found that, due to the short lifetime of Chl*, the formation of $^3$Chl* state is dramatically reduced, which would result in a decrease of the consequent production of $O_2$* in the $b_6f$ complex. It was inferred that excitation-induced ET interaction with nearby aromatic amino acid residue(s) is the most likely explanation of the observed effect. Based on the new structure data, it is proposed that the local structure around the Chl $a$ facilitates rapid quenching of Chl* and thereby minimizes the formation of singlet oxygen.

## 4.2. Conserved Geometry of the Chl $a$ Binding

According to the high-resolution crystallographic structures (Kurisu et al. 2003; Stroebel et al. 2003) of the cyt $b_6f$ complex, the monomeric Chl $a$ molecule is bound between helices F and G of subunit IV, with the phytyl tail threaded through the portal connecting the electropositive $Q_p$ quinone binding niche, and the central quinone-exchange cavity (Fig. 1.4A). The chlorin ring of the Chl $a$ is parallel to the plane of the heme $b_n$, which is separated by approximately 16 Å center-to-center from the Chl $a$, whereas the β-carotene molecule near the center of the transmembrane region is approximately 14 Å (the closest distance) from the Chl $a$ (Fig. 4.1). These geometrical configurations of the Chl $a$ binding are essentially identical in both crystal structures obtained from two species, whose appearance in evolution is separated by $10^9$ years.



**Fig. 4.1** The nanospace of the monomeric Chl $a$ molecule in the cyt $b_6f$ complex. Edge-to-edge distances (Å) to three closest TYR and TRP residues are specified in the context of ET (Hanson 1990; Moser et al. 1995; Page et al. 1999).
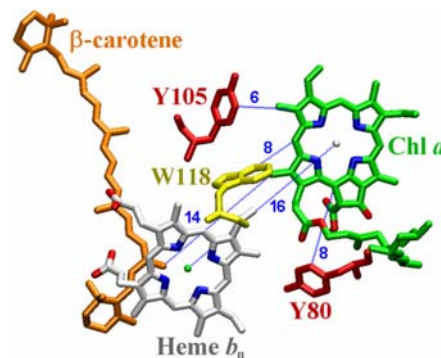
## 4.3.  Absorption Spectra of the Cyt $b_6f$ Complexes

The absorbance spectra of the cyt $b_6f$ complexes are shown in Fig. 4.2A. The differences in the absorbance spectra observed in the spectral region of 630–700 nm reflect slightly different optical properties of the Chl *a* molecule in these samples and may indicate that the local protein structures around the Chl *a* vary for complexes isolated from different species (Fig. 4.2A, inset). The Chl *a* $Q_y$ bands in the ML$b_6f$-crystal and SC$b_6f$ complexes maximize at 671.5 nm and have fwhm of 17 nm, whereas in the ML$b_6f$ and Sp$b_6f$ complexes, the $Q_y$ band of Chl *a* is centered at 671.5 nm and 668 nm and have fwhm of 20 nm and 17 nm, respectively. The absorbance of the Chl *a* in the Sp$b_6f$ is similar to that in the $b_6f$ complex of *C. reinhardtii* reported by Pierre et al. (1997). The Chl *a* $Q_y$ absorption band at room temperature did not depend on the redox state of the cyt $b_6f$ complex, as it was not affected by the addition of dithionite, ascorbate, or ferricyanide.
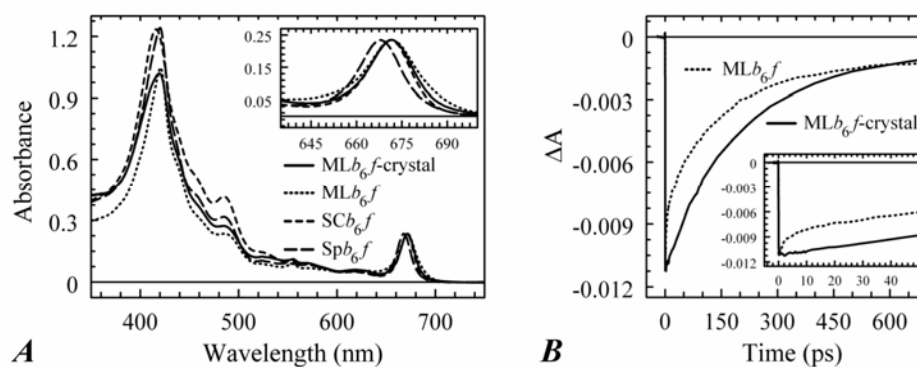


**Fig. 4.2** (A) The absorbance spectra of the cyt $b_6f$ complexes purified from *Mastigocladus laminosus* (ML$b_6f$), *Synechococcus* PCC 7002 (SC$b_6f$), Spinach chloroplast (Sp$b_6f$), and dissolved diffraction quality crystals of the cyt $b_6f$ complex from *Mastigocladus laminosus* (ML$b_6f$-crystal). (B) Time-resolved transient absorption difference profiles probed at 680 nm after excitation at 660 nm for the conventionally purified cyt $b_6f$ complex (ML$b_6f$), and dissolved single crystals (ML$b_6f$-crystal).

## 4.4.  Ultrafast Kinetics of the Chl *a* Singlet Excited State

The ultrafast kinetics of the singlet excited state of the monomeric Chl *a* in the cyt $b_6f$ complexes from the four studied samples were probed by femtosecond time-resolved pump-probe spectroscopy. The samples were excited at 660 nm and absorbance

difference kinetics were recorded at 5 nm intervals at multiple probe wavelengths covering the entire $Q_y$ absorption band of the Chl *a* between 665 nm and 695 nm.

*Stoichiometry of Chl a in the cyt $b_6f$ complex is critical for unambiguous interpretation of the results.* Purified preparations of the cyt $b_6f$ complexes in active dimeric form usually contain non-specifically bound Chl *a*. Depending on the preparation, these contaminant Chl *a* molecules may account for ~20% of the total Chl *a* contents in the cyt $b_6f$ complexes. Our optical experiments cannot distinguish the signals arising from the native intrinsic Chl *a* from signals that stem from the contaminant Chl *a* that would obscure interpretation of the data. To ensure highest sample purity and to simplify the data analysis, we performed ultrafast pump-probe experiments on the cyt $b_6f$ complex from a sample, "ML$b_6f$-crystal", obtained by re-dissolving approximately sixty diffraction quality single crystals.

Fig. 4.2B shows the absorption difference kinetics for the ML$b_6f$ complexes purified by conventional means, probed at 680 nm after exciting a sample at 660 nm, and that for the ML$b_6f$-crystal complexes purified through crystallization. Visual inspection of the two profiles and the exponential fits to the data reveal major differences. The $\Delta A$ kinetics of the dissolved single crystals can be described by one major decay component of 194 ps (91.2%) accompanied by a weak 5.5 ns (8.8%) component (the respective amplitudes are given in brackets). The optimized fit of the profile obtained for the ML$b_6f$ complex purified by conventional means requires at least three decay components: 6.5 ps (24.6%), 153 ps (62.4%), and 5.5 ns (13%). The main component in the crystal-purified sample is 194 ps and thus it can be ascribed to the ground state recovery process of the intrinsic Chl *a* in the $b_6f$ complex. The 6.5 ps component is not present in the $\Delta A$ signal measured for the ML$b_6f$-crystal, and therefore can be ascribed entirely to the contaminant Chl *a*. The longest component lifetime of 5.5 ns could not be reliably determined due to the limited time window. It was, however, similar to the lifetime of monomeric Chl *a* in solution (Seely and Connolly 1986), and it is attributed to a small fraction of Chl *a* molecules whose excited state properties were not affected by the environment.

The $\Delta A$ kinetics for the SP$b_6f$ could be described with three components similar to the ones obtained by fitting the data for the ML$b_6f$ complexes, indicating that the dynamics

of the Chl *a* excited state in these species are very similar.  In contrast, the Δ*A* profiles for the SC*b₆f* complexes could be fit with a single decay component with a lifetime of 230 ps, implying that the monomeric inactive complexes contain a significantly smaller pool of non-specifically bound Chl *a*.
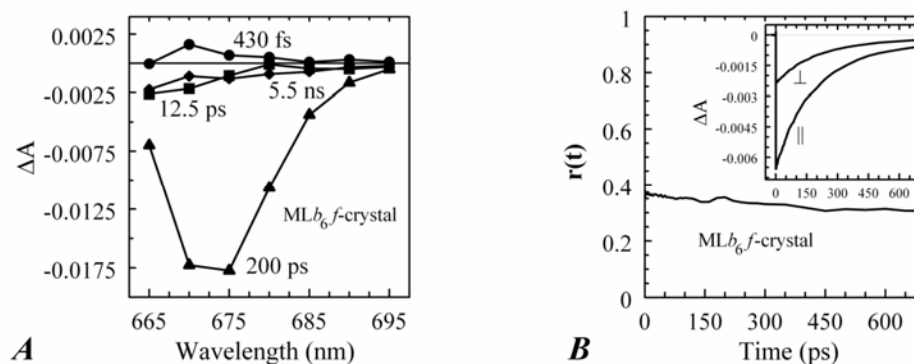


**Fig. 4.3** (A) Decay-associated spectra obtained by global analysis of Δ*A* profiles for the dissolved single crystals of the ML*b₆f*-crystal. (B) Time-resolved anisotropy of Δ*A* signal probed at 680 nm for the ML*b₆f*-crystal. Inset: corresponding anisotropic Δ*A*∥ and Δ*A*⊥ profiles.

*Global analysis of ultrafast time-resolved absorption difference profiles.* All time-resolved Δ*A* profiles for the ML*b₆f*-crystal complex probed at several wavelengths between 665 nm and 695 nm could be fit globally with four common decay components having lifetimes of 430 fs, 12 ps, 200 ps, and 5.5 ns. The probe-wavelength-dependent amplitudes of these components were assembled into the decay-associated spectra (DAS) shown in Fig. 4.3A. The DAS are dominated by the 200 ps component, which corresponds to the monomeric Chl *a* ground state recovery kinetics, as its spectral shape is consistent with the photobleaching spectrum of the monomeric Chl *a*. The amplitudes of the DAS of the 12 ps and 5.5 ns components are small and their spectral shapes are broad. We ascribe these components to a small heterogeneous pool of non-specifically bound Chl *a*. Similar DAS components with larger amplitudes were observed in the absorption difference profile of the ML*b₆f* complex, which had a higher concentration of non-specifically bound Chl. The global analysis also yielded a 430 fs component, which can be attributed to vibrational relaxation of the Chl* that is known to occur on this time

scale (Savikhin and Struve 1994). The global analysis of the transient time-resolved absorption difference profiles for the SC$b_6f$ and Sp$b_6f$ yielded similar decay times.

*Ultrafast time-resolved anisotropy*. Stroebel et al. (2003) suggested that the Chl *a* could facilitate interaction with other components of the photosynthetic apparatus. The plane of the Chl *a* may be, for example, "twisted" in response to absorption of light and cause structural response of the protein that could propagate through the cyt *b*$_6$*f* and signal proteins, e. g., LHC kinase, on the stromal side of the membrane. To test that hypothesis, we monitored the orientation of the Chl *a* in excited state by measuring the anisotropy *r(t)* of the Δ*A* signal probed by polarized light at wavelength ranging from 665 nm to 695 nm after excitation of the complex at 660 nm. The anisotropy dynamics showed negligible dependence on the probe wavelength, and only one trace measured at 680 nm for the ML$b_6f$-crystal complex is shown in Fig. 4.3B. The anisotropy is 0.37, which is close to the theoretical maximum of 0.4 for a completely rigid molecule with parallel absorption and emission transition dipole moments. It is almost constant during the lifetime of the Chl *a* excited state indicating that, during this time (~200 ps), Chl *a* excitation does not lead to detectable reorientation of the molecule.

## 4.5.   Irreversible Photodegradation of the Monomeric Chl *a*

The level of Chl *a* photoprotection in the cyt *b*$_6$*f* complex was evaluated under aerobic conditions by monitoring irreversible photodegradation of the Chl *a* in the ML$b_6f$ complex and comparing it with the photodegradation kinetics of monomeric Chl *a* dissolved in organic solvents. Monomeric Chl *a* dissolved in organic solvents exhibited photodegradation kinetics similar to the kinetics previously observed (Jen and MacKinney 1970). The profiles can be fit with two exponential components, indicating that the degradation occurs with two characteristic lifetimes of 6 minutes and 2 hrs. The photodegradation kinetics of the Chl *a* in the ML$b_6f$ complex also exhibits two exponential decay components but with much longer lifetimes of 14 hrs and 260 hrs. Thus, the Chl *a* in the ML$b_6f$ complex is 130–140 times more stable than in solution.

4.6.   Discussion and Analysis

*Steady state absorbance spectra reflect the Chl a local environment.* The Chl *a* $Q_y$ absorbance band for the $b_6f$ complexes from Sp (Sp$b_6f$) (Fig. 4.2A, inset) and from *C. reinhardtii* (Pierre et al. 1997) are blue-shifted by ~3.5 nm with respect to the absorbance bands of the Chl *a* in the SC$b_6f$ and ML$b_6f$ (Fig. 4.2A, inset). Based on structural analysis, we propose that this difference in the Chl *a* $Q_y$ absorption band positions may stem from the different strength of $\pi$-electrostatic interaction between the Chl *a* and surrounding aromatic amino residues in these species. The noticeable broadening of the Chl *a* $Q_y$ band in the ML$b_6f$, if compared to the ML$b_6f$-crystal, most probably arises from the presence of an inhomogeneous pool of non-specifically bound Chl *a* molecules in the ML$b_6f$ sample purified by conventional methods.

*Unusually short lifetime of the singlet excited state of the Chl a.* Peterman et al. (1998) reported that the singlet excited state of the Chl *a* in the functionally inactive monomeric cyt $b_6f$ complex of *Synechocystis* PCC 6803 decays in 250±20 ps, compared to the 5–6 ns lifetime reported for the monomeric Chl *a* molecules in solution (Seely and Connolly 1986). Our experiments confirmed that the unusually short Chl* lifetime is also characteristic of the enzymatically active dimeric $b_6f$ complexes of *M. laminosus* and spinach, as well as inactive monomeric complexes from *Synechococcus* PCC 7002 suggesting, unexpectedly, that the local environment of the Chl *a* is similar in both active and inactive forms of the $b_6f$ complex. In the following, we will discuss three possible mechanisms that may cause the observed rapid quenching of Chl* *a*: (*i*) increased rate of intersystem crossing, (*ii*) interaction with the heme, and (*iii*) excitation induced ET between the Chl *a* and nearby amino acid residue(s).

(*i*) *Increased rate of intersystem crossing.* To account for the observed ~200 ps excited state lifetime of the Chl *a* in the $b_6f$ complex, the local protein environment must increase the intersystem crossing rate 40–50 fold, which would result in Chl *a* triplet formation with 98% efficiency. Since the triplet excited state lifetime is ~200 ns under aerobic conditions (Fujimori and Livingston 1957), this will also significantly delay the recovery of the Chl *a* ground state. Our absorbance difference measurements, however, show that the recovery of the Chl *a* ground state in the $b_6f$ complex occurs within ~200 ps

and rules out the possibility that any significant amount of Chl $a$ triplet state can be formed. Thus, we can rule out intersystem crossing as a possible mechanism responsible for the unusually short singlet excited state lifetime of the Chl $a$.

(*ii*) *Interaction with the nearby heme.* According to high-resolution crystal structures of the cyt $b_6f$ complex (Kurisu et al. 2003; Stroebel et al. 2003), the heme $b_n$ of cyt $b_6$ is parallel to the chlorin ring of the Chl $a$, from which it is separated by 16 Å (Fe-Mg center-to-center distance, Fig. 4.1). However, dithionite reduction of the initially oxidized heme revealed no dependence of the Chl* lifetime on the redox state of the nearby hemes, ruling out the involvement of the heme in the quenching process. Similar results were obtained by Peterman et al. (1998) for the enzymatically inactive $b_6f$ complexes.

(*iii*) *Excitation induced ET between the Chl a and nearby aromatic amino acid residues.* It has been demonstrated by several groups (Karen et al. 1983; Visser et al. 1987; Mataga et al. 2000; Zhong and Zewail 2001) that in flavin-binding proteins the electronic excited state of a chromophore can be efficiently quenched via ET exchange with a nearby aromatic amino acid residue. The possible involvement of aromatic residues in fluorescence quenching of bacteriochlorophyll and Chl molecules was also discussed by Li et al. (1997) and Peterman et al. (1998).

The sequence of ET events that may lead to quenching of Chl* $a$ is depicted in the redox potential diagram shown in Fig. 4.4A. When a Chl $a$ molecule is excited its electron donating (oxidation) potential (Chl/Chl$^{\bullet+}$) becomes more negative, while its electron accepting (reduction) potential (Chl/Chl$^{\bullet-}$) becomes more positive by a value approximately equal to the singlet excitation energy (Watanabe and Kobayashi 1990; Jones and Fox 1994; Oda et al. 2001). The energy of the $Q_y$ transition of the Chl $a$ is ~1.85 eV and using the Chl/Chl$^{\bullet-}$ of −0.88 V (Watanabe and Kobayashi 1990) the electron accepting Chl*/Chl$^{\bullet-}$ potential becomes anodic enough to initiate the first ET step from nearby Tyr residue since the Tyr/Tyr$^{\bullet+}$ electron donating potential is about +0.93 V (Harriman 1987; DeFelippis et al. 1989; Jovanovic et al. 1991). Once an electron is transferred from the Tyr to the Chl*, the singlet excited state of the Chl $a$ is transformed into a non-fluorescent reduced Chl$^-$ state. The electron accepting Chl/Chl$^{\bullet-}$ potential is, however, significantly more negative than the electron donating Tyr/Tyr$^{\bullet+}$

potential, forcing ET from the reduced $Chl^-$ back to the $Tyr^+$. As the result, both reactants return to their neutral ground states.

**Fig. 4.4** (A) The proposed quenching mechanism of Chl* *a* by excitation induced ET process. Absorption of a photon promotes the Chl *a* into its singlet excited state and rises the oxidation potential from –0.88 V to +0.97 V (wavy arrow). In the following quenching process, the electron is first donated by a nearby Tyr to Chl*, transforming Chl* into unexcited $Chl^-$ state (arrow 1). In the second ET step (arrow 2), the $Chl^-$ donates electron to $Tyr^+$, resulting in neutral Chl and Tyr and completing the quenching process. (B) Similar scenario proposed for fluorescence quenching of the riboflavin (RF) in riboflavin-binding protein with the experimentally measured lifetimes of ET (Mataga et al. 2000; Zhong and Zewail 2001).
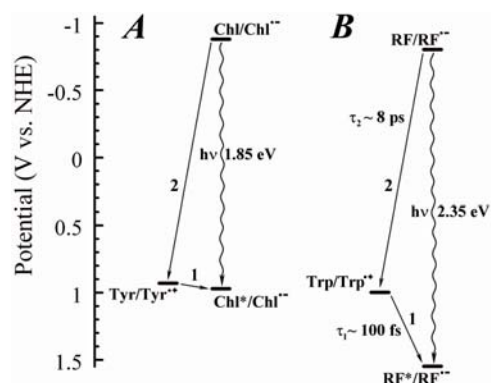


This model of the quenching kinetics of the singlet excited state of the Chl *a* can be described by the following sequential ET scheme:
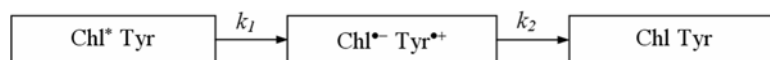


where $k_1$ and $k_2$ are the intrinsic rates of the respective ET processes denoted by arrows "1" and "2" in Fig. 4.4A. To reproduce the essentially single-exponential $\Delta A$ kinetics measured at ~670 nm in the proposed scenario, the rate of the first ET $k_1$ should be close to $(200 \text{ ps})^{-1}$, while the rate of the second ET step $k_2$ should be faster than $\sim(150 \text{ ps})^{-1}$.

The mechanism of ET and underlying theory have been described in Section 3.2. In the following, we used the Moser-Dutton semi-empirical relationship (Eq. 3.17) to estimate the rates of exothermic ET for steps 1 and 2 (Fig. 4.4A). By comparing the values of $R$ and $\Delta G^0$ for all nearest aromatic residues we inferred that Tyr105 ($R$=6 Å, Fig. 4.1) is the most likely residue responsible for electron-transfer mediated quenching of the Chl *a* excited state. Using a value of $\lambda = 0.7$ eV for the reorganization energy (Page et al. 2003), Eq. 3.17 predicts a rate of $k_1$=$(234 \text{ ps})^{-1}$ for the first ET step, which is in good agreement with the experimental value $(200 \text{ ps})^{-1}$. However, this equation results in the rate constant $k_2$=$(0.8 \text{ μs})^{-1}$ for the second ET, which is 4 orders of magnitude slower

than the observed recovery rate of the Chl *a* ground state. This dramatic discrepancy may stem from uncertainties in reorganization energy and/or redox potential values. For example, using $\lambda$ = 1.05 eV (still within the range of 0.9±0.2 eV, cited by Page et al. 2003), Eq. 3.17 results in a rate of $(140 \text{ ps})^{-1}$ for the second ET, which is not inconsistent with the experimental results.

Similar high electron back-transfer rates to amino acid residues have been measured for the ET mediated fluorescence quenching of the riboflavin (RF) in riboflavin-binding protein (Mataga et al. 2000; Zhong and Zewail 2001). The $RF/RF^{\bullet-}$ redox potential (–0.8 V, Fig. 4.4B) is very close to that of the $Chl/Chl^{\bullet-}$ (–0.88 V, Fig. 4.4A), which makes the comparison between these two cases especially relevant. Using transient absorption and fluorescence spectroscopy, Zhong and Zewail (2001) determined that the first and second ET steps occur with lifetimes ~100 fs and ~8 ps, respectively (Fig. 4.4B) and proposed that ET exchange with the nearby Trp residue was responsible for the quenching of the RF excited state. The $Trp/Trp^{\bullet+}$ potential is 1.03 V (Harriman 1987; DeFelippis et al. 1991), $R$=3.7 Å and, using $\lambda$ = 0.7 eV, Eq. 3.17 yields lifetimes of 160 fs and 52 ns for the first and second ET steps, respectively. As in the case of the Chl *a* and Tyr105 in the cyt $b_6f$ complex, the kinetics of the first ET step in riboflavin-binding protein is described very well by Eq. 3.17, but the rate calculated for the second ET step is 4 orders of magnitude slower than the measured value. Agreement could, however, be attained if a reorganization energy $\lambda$ = 1.04 eV is used for the second ET step. This value of the reorganization energy is consistent with a value of $\lambda$ = 1.05 eV for the $Chl^-\rightarrow Tyr^+$ ET step required to reproduce the experimental data by the proposed kinetic model. It was concluded that the ET mediated quenching is the most plausible mechanism responsible for the unusually short lifetime of Chl* *a* in the cyt $b_6f$ complex.

*Photochemical degradation of the Chl a in the cyt $b_6f$ complex and protection against singlet oxygen formation*. Using triplet-triplet energy transfer theory described in (Dexter 1953) and data published elsewhere (Schödel et al. 1998; Bodunov and Berberan-Santos 2004), we estimated that triplet-triplet energy transfer from $^3Chl^*$ to $^3Car^*$ in the $b_6f$ complex should occur in ~0.3 ms, which is much too slow to compete with singlet

oxygen formation. Thus, the conventional mechanism of singlet oxygen protection by the direct triplet-triplet energy transfer process does not apply to the cyt $b_6f$ complex.

## 4.7. Conclusion

While the β-carotene is too far from the Chl $a$ for direct protection, our photodegradation experiments demonstrate that the Chl $a$ in the $b_6f$ complex is 130–140 times more stable than in solution. We propose that protection, at least in part, is realized through specific arrangement of the local protein environment of the Chl $a$ to ensure rapid quenching of Chl*. Shortening of the Chl* lifetime from 5–6 ns to 200 ps causes a 25–30 fold decrease in the quantum yield of the $^3$Chl* state formation, and thus reduces the rate of $O_2$* formation. To the best of our knowledge, this mechanism of Chl protection against singlet oxygen formation has not been yet reported. The unusually short singlet excited state lifetime of the Chl $a$ in the cyt $b_6f$ complex can account only for 25–30 fold protection, while our experiments reveal that Chl $a$ in the complex is 130–140 times more stable than monomeric Chl $a$ in solution. This implies that one or more additional unconventional protection mechanism(s) exist in the cyt $b_6f$ complex.

# CHAPTER 5.  ASYMMETRIC ELECTRON TRANSFER IN PS I

Point mutations were introduced near the primary electron acceptor sites assigned to $A_0$ in both the PsaA and PsaB branches of PS I in the cyanobacterium *Synechocystis sp.* PCC 6803. The residues Met688$_{PsaA}$ and Met668$_{PsaB}$, which provide the axial ligands to the $Mg^{2+}$ of the eC-A3 and eC-B3 chlorophylls, were changed to leucine and asparagine (Chl notation follows, Jordan et al. 2001). The removal of the ligand is expected to alter the midpoint potential of the $A_0/A_0^-$ redox pair and result in a change in the intrinsic charge separation rate and secondary ET kinetics from $A_0^-$ to $A_1$. The dynamics of primary charge separation and secondary ET was studied at 690 nm and 390 nm in these mutants by ultrafast optical pump-probe spectroscopy. The data reveal that mutations in the PsaB-branch do not alter ET dynamics, whereas mutations in the PsaA-branch have a distinct effect on ET, slowing down both the primary charge separation and the secondary ET step (the latter by factor of 3 to 10). These results suggest that ET in cyanobacterial PS I is asymmetric and occurs primarily along the PsaA branch of cofactors.

This chapter is based on the following manuscripts:

Dashdorj N., W. Xu, R.O. Cohen, J.H. Golbeck and S. Savikhin. 2005. Asymmetric electron transfer in cyanobacterial photosystem I: Charge separation and secondary electron transfer dynamics of mutations near the primary electron acceptor $A_0$. *Biophys. J.* 88:1238-1249.

Dashdorj N., W. Xu, R.O. Cohen, J.H. Golbeck and S. Savikhin. 2005. Probing the active electron transfer branch in the photosystem I reaction center from *Synechocystis* sp. PCC 6803. *In* Photosynthesis: Fundamental Aspects to Global Perspectives. A. van der Est and Bruce D., Editors, ACG Publishing, Lawrence, KS, U.S.A. 30-33.

## 5.1. On the Presence of Two Symmetrical Branches

The presence of two highly symmetrical branches of cofactors in the PS I RC (Fig. 1.7) raises the question of whether one or both are active in ET under physiological relevant conditions. There is widespread agreement in the field that the PsaA-branch of cofactors is active in both prokaryotes and eukaryotes. Evidence that the PsaB-branch of cofactors is equally active has mainly been obtained in eukaryotes such as in the algae *C. sorokiniana* (Joliot and Joliot 1999) and *C. reinhardtii* (Boudreaux et al. 2001; Fairclough et al. 2001; Guergova-Kuras et al. 2001; Muhiuddin et al. 2001), while evidence indicating significantly less PsaB-branch ET has been reported in prokaryotes such as the cyanobacteria *Synechococcus* sp. PCC 7002 and *Synechocystis* sp. PCC 6803 (Golbeck et al. 2001; Xu et al. 2003a; Xu et al. 2003b). These conclusions have been based primarily on studies involving specific mutations around the respective phylloquinone ($A_1$) binding sites on the PsaA and PsaB polypeptides. The advantage to these mutations is that the spectral and functional changes they induce are so subtle that they are not expected to influence the initial charge separation. The disadvantage is that the subtle nature of the changes induced by these mutations leaves some ambiguity in the interpretation of the data. Moreover, these experiments have focused primarily on measurements of changes in the ET kinetics (optical and EPR), which reflect the relatively slow ET step from the $A_1$ to $F_X$. In this case, the $F_X$ electron acceptor is common to both branches, and the changes around $A_1$ in one branch can, in principle, influence the properties of $F_X$ and thereby affect the ET kinetics through the other branch.

In this study, we applied optical femtosecond pump-probe techniques to study ET in two complimentary pairs of point mutants, in which Met688$_{PsaA}$ or Met668$_{PsaB}$ were replaced by Leu (Cohen et al. 2004) or Asn (R. Cohen et al., manuscript in preparation) in *Synechocystis* sp. PCC 6803. These Met residues are proposed to provide the axial ligands to the respective $Mg^{2+}$ ions of the two $A_0$ chlorophyll molecules. The Met ligand to $Mg^{2+}$ is expected to be weak, and the possibility that no axial ligand exists also needs to be considered (Goldsmith et al. 1996). However, regardless of the nature of the interaction between the Met residues and the chlorophylls, their proximity to one another means that a mutation in the amino acid will likely alter the midpoint potential of the

$A_0/A_0^-$ redox pair. This should result in a change in Gibbs free energy associated with both primary charge separation and the secondary ET step due to a change in the Frank-Condon factor in the Marcus equation, which relates the rate of ET to changes in Gibbs free energy and reorganization energy (Moser et al. 1992). We will show that the mutations on the PsaA side have a pronounced effect on the primary charge separation and especially on the secondary ET kinetics, while the corresponding mutations on the PsaB side have a minimal effect on the ET process. These results support previous suggestions that forward ET in cyanobacterial PS I is asymmetric and occurs predominantly along the PsaA-branch of cofactors.

## 5.2. $P700^+ - P700$ Difference Spectra

The $P700^+ - P700$ difference spectra of the mutants are presented in Fig. 5.1. Noticeable deviations from the wild-type (WT) spectra are observed in the region of the relatively narrow (fwhm~11 nm) absorption band centered at ~690 nm, denoted as C690 in (Savikhin et al. 2001) and tentatively ascribed to the absorption from the neutral monomeric Chl $a$ that emerges from P700 when one of the pigments in this special pair becomes oxidized. While the C690 feature encounters relatively minor changes when the mutations are introduced near $A_0$ in the PsaB-branch (Fig. 5.1B), the amplitude of this band decreases almost two-fold when the mutations are introduced near $A_0$ in the PsaA-branch (Fig. 5.1A).
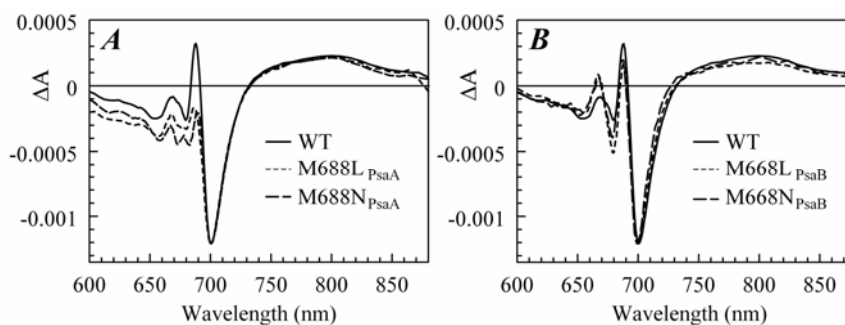


**Fig. 5.1** $P700^+ - P700$ absorption difference spectra of PS I complexes with mutations in the PsaA-branch (A) and in the PsaB-branch (B). Positive-going bands in both panels represent steady state absorption spectrum of PS I complexes in arbitrary units.

The integrated deviations from the $P700^+-$ P700 spectra of WT are 1.5 times larger in the PsaA-branch mutants than in the PsaB-branch mutants, suggesting that the eC-A3 chlorophyll is more strongly coupled to the rest of the pigments in the RC than is the eC-B3 chlorophyll.

## 5.3.  The $A_0$ Electronic Absorption Spectra

The transient $(A_0^- - A_0)$ absorption difference spectra of PS I from the $M688L_{PsaA}$, $M688N_{PsaA}$, $M668L_{PsaB}$ and $M668N_{PsaB}$ mutants were obtained by exciting the samples at 660 nm, the blue edge of the core antenna spectrum, and sweeping the probe wavelength from 660 nm to 720 nm at fixed time delays. Fitting the $(A_0^- - A_0)$ absorption difference spectra of the PsaB-side mutants as described in (Savikhin et al. 2001) reveals that the positions and widths of the $A_0$ absorption bands are respectively 685.2 nm and 11 nm fwhm in PS I complexes from the $M668L_{PsaB}$ mutant, and 686.6 nm and 10 nm fwhm in PS I complexes from the $M668N_{PsaB}$ mutant. Within the error of our experiment, these parameters are essentially the same as measured earlier for PS I complexes from WT (685.7 nm and 11 nm, Savikhin et al. 2001). The best fits to the $(A_0^- - A_0)$ absorption spectra of the PsaA-side mutants reveal that the $A_0$ band positions and widths are respectively 688.6 nm and 11.6 nm fwhm in PS I complexes from the $M688L_{PsaA}$ mutant and 683.7 nm and 15.6 nm fwhm in PS I complexes from the $M688N_{PsaA}$ mutant (data not shown). The $A_0$ band of the $M688L_{PsaA}$ mutant is therefore ~3 nm red-shifted and that of the $M688N_{PsaA}$ mutant is ~2 nm blue-shifted with respect to the $A_0$ band position measured in WT.

## 5.4.  Probing Formation of $A_1^-$ by near UV Pump-Probe Spectroscopy

The formation of the semiquinone state of the secondary electron acceptor $A_1$ can be monitored directly by its broad near-UV absorption band around 390 nm (Lüneberg et al. 1994; Brettel and Vos 1999). The time-resolved absorption difference spectra of WT PS I with open and closed RCs were recorded at 390 nm after exciting at 660 nm under annihilation free regime for the first time.
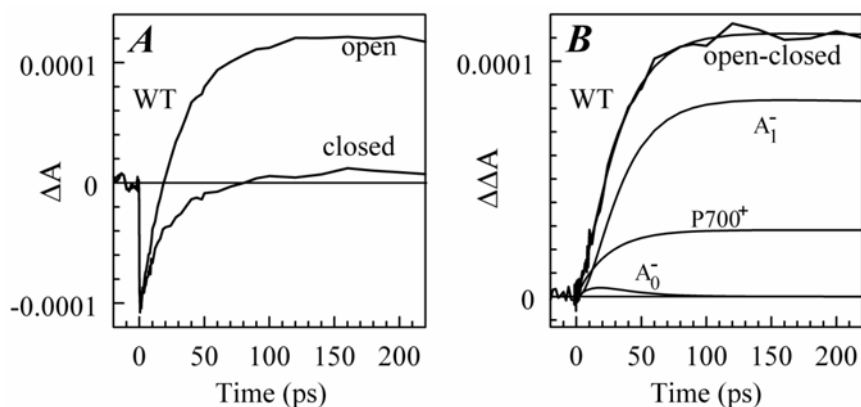
**Fig. 5.2** Time-resolved absorption difference profiles for WT PS I complex excited at 660 nm and probed at 390 nm. Negative going signals indicate photobleaching/stimulated emission. (A) Time-resolved absorption difference profiles obtained for PS I complexes with open and closed RC. (B) Time-resolved (open-closed) absorption difference profile, optimized fit to it using ETM, and signal contributions due to the formation of $P700^+$, $A_0^-$ and $A_1^-$.

In Fig. 5.2B the $\Delta\Delta A$ profile was obtained by subtraction of the $\Delta A$ profile for closed RC from that for open RC. As the result, the negative early time component which stems from excited antenna pigments was eliminated (Savikhin et al. 2001). The $\Delta\Delta A$ profile was then fitted within a simple sequential energy/electron transfer model (ETM) shown below and similar to (Savikhin et al. 2001):
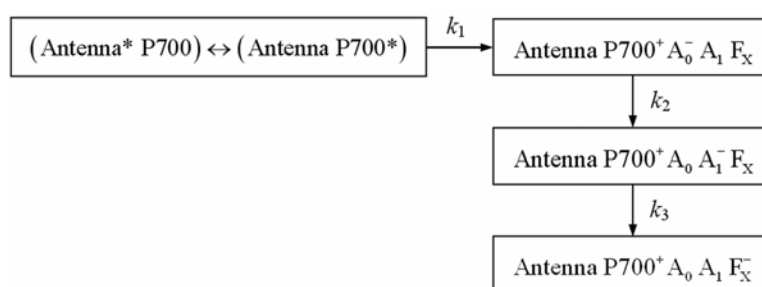


where $k_1$ is the effective charge separation rate, which encompasses the cumulative effects of antenna excitation equilibration, trapping at P700, back-transfer from P700* to the antenna complex and the primary charge separation; $k_2$ is the intrinsic rate of the secondary ET $A_0^- \rightarrow A_1$, and $k_3$ is the intrinsic rate of the following ET step $A_1 \rightarrow F_X$. In our simulations the effective excitation trapping rate $k_1$ was fixed at $(24 \text{ ps})^{-1}$ in accordance with (Savikhin et al. 2001), the intrinsic ET rate $k_3$ was assumed to be long

compared to the studied time window (van der Est et al. 1994; Brettel 1998; Sakuragi et al. 2002), and the ratio between the signals due to the formation of $P700^+A_0A_1^-$ and $P700^+A_0A_1F_X^-$ was set to 3:1 as measured in (Brettel 1988). Best fit to the (open-closed) profile shown in Fig. 5.2 was obtained with $k_2 = (12.8\ ps)^{-1}$; reasonable fits could be obtained with $k_2 = (8\ldots15\ ps)^{-1}$, which is consistent with our previous results derived from global analysis of the (open-closed) profiles in Chl $a$ absorption spectral region (Savikhin et al. 2001). Fig. 5.2B also shows the modeled signal due to the formation of each of the intermediate states.
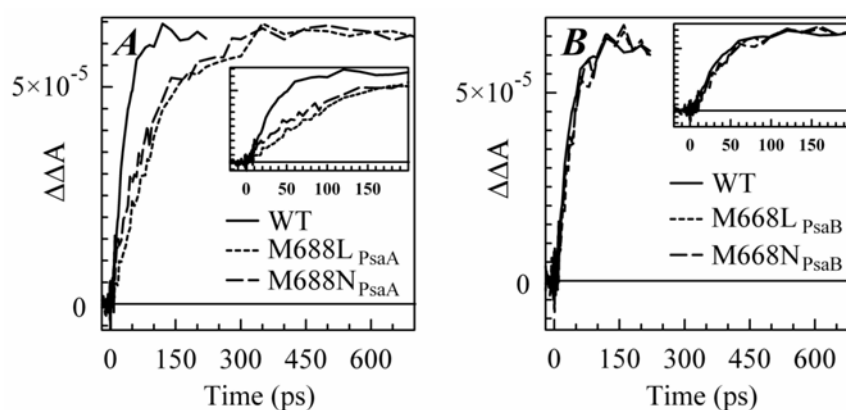


**Fig. 5.3** Time-resolved (open-closed) absorption difference profiles for WT, M688L$_{PsaA}$ and M688N$_{PsaA}$ mutants (A), and for WT, M668L$_{PsaB}$ and M668N$_{PsaB}$ mutants (B). All samples were excited at 660 nm and absorption differences were probed at 390 nm.

The time-resolved (open-closed) profiles measured for PsaB-side mutants are almost superimposable on that of the WT as seen in Fig. 5.3B, suggesting that the rate of secondary ET $k_2$ is unaffected by mutations on the PsaB-branch of the RC. However, the $A_1^-$ formation kinetics were dramatically altered in PS I complexes in which the mutations were introduced on the PsaA-branch of the RC (Fig. 5.3A). The fits to the (open-closed) profiles shown in Fig. 5.3A revealed that the intrinsic time of the ET from $A_0$ to $A_1$ is $112\pm10$ ps and $100\pm10$ ps in the M688N$_{PsaA}$ and M688L$_{PsaA}$ mutants, respectively, which is almost an order of magnitude slower than secondary ET in the WT.

## 5.5. Probing the Kinetics of $A_0^-$ Absorption

According to (Savikhin et al. 2001), the (open-closed) $\Delta\Delta A$ profile probed at 690 nm is especially informative as it closely follows the dynamics of formation and decay of the $A_0^-$ state. At this particular wavelength, the initial rise of PB is primarily due to the formation of $A_0^-$ state, since the $(A_0^- - A_0)$ spectrum has a maximum PB at ~686 nm (Hastings et al. 1994; Savikhin et al. 2001).
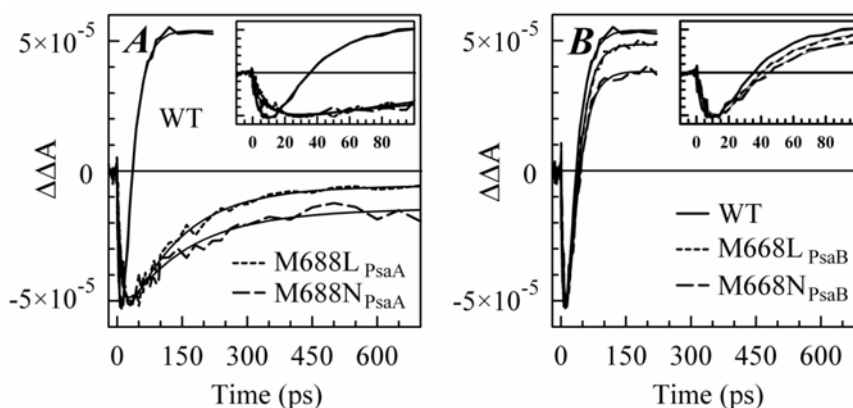


**Fig. 5.4** Time-resolved (open-closed) absorption difference profiles for WT, M688L$_{PsaA}$ and M688N$_{PsaA}$ mutants (A), and for WT, M668L$_{PsaB}$ and M668N$_{PsaB}$ mutants (B). All samples were excited at 660 nm and absorption differences were probed at 690 nm.

Fig. 5.4B shows the (open-closed) $\Delta\Delta A$ profile measured at 690 nm for PS I complexes from the WT (Savikhin et al. 2001) and the M668L$_{PsaB}$ and M668N$_{PsaB}$ mutants. The only change in the case of the PsaB-side mutants is the level of the residual absorption, which is consistent with the lower $(P700^+ - P700)$ absorption level at 690 nm in the mutants as shown in Fig. 5.1B. Simple two-exponential fit to the $\Delta\Delta A$ profiles reveals a ~10 ps PB rise followed by a ~24 ps PB decay for all three curves, suggesting that the PsaB-side mutations do not influence ET in the PS I RC.

As in the case of the 390 nm pump-probe profiles, dramatic differences were observed in the $\Delta\Delta A$ signals measured for the PsaA-side mutants at 690 nm (Fig. 5.4A, notice the time-scale change). Biexponential fits to these profiles reveal ~11.4 ps and

~10.4 ps PB rise times, combined with 130±20 ps and 145±20 ps PB decay times for the M688L$_{PsaA}$ and M688N$_{PsaA}$ mutants, respectively.

## 5.6.    Global Analysis of Pump-Probe Kinetics

Pump-probe profiles for PS I complexes with open RC from all mutants were measured as a function of probe wavelength and analyzed globally to produce decay-associated spectra (DAS) as described in (Savikhin et al. 2000). The excitation (pump) wavelength was set to 660 nm and the probe wavelength was varied in the range 650–720 nm.

The pump-probe profiles for PS I complexes from the PsaB-side mutants were essentially the same as for complexes from the WT and could be described by 4 major components (Fig. 5.5A) (Savikhin et al. 2000). The two shortest DAS components have been previously assigned to excitation equilibration in the PS I antenna, the ~24 ps DAS component was identified as effective energy trapping by the RC, and the residual long-time (>1 ns) component was ascribed to the (P700$^+$– P700) absorption difference.

Global fits to pump-probe profiles obtained for PS I complexes from the PsaA-side mutants were only possible with 5 distinct decay components (Fig. 5.5). Within the error of the experiment, the DAS for the two shortest components for the PsaA-side mutants are almost identical to the two shortest components found in the WT, and can be assigned to excitation equilibration among antenna pigments. The spectral shape of DAS of the ~30 ps component is qualitatively similar to the ~24 ps component found in WT and it can be attributed to the effective energy trapping rate, which is somewhat slower in the PsaA-side mutants. Similarly, we attribute the long (>1 ns) component to the (P700$^+$– P700) absorption difference (compare to Fig. 5.1A).

While there may be subtle differences in the DAS between the PsaA-side and PsaB-side mutants, the important difference is the presence of an additional kinetic component in the PsaA-side mutants. The DAS of the additional fifth (102 and 210 ps) component has a fwhm of 11–15 nm and is centered at 689±1 and 684±1 nm in the case of PS I complexes from the M688L$_{PsaA}$ and M688N$_{PsaA}$ mutants, respectively. Its spectral shape is consistent with the PB spectrum of a single Chl $a$ molecule, and we attribute this component to the decay of the A$_0^-$ state, which reflects ET from A$_0^-$ to A$_1$. In the WT and

PsaB-side mutants, the ET from $A_0^-$ to $A_1$ is too fast (~13 ps) compared to the overall antenna decay (~24 ps), and could not to be distinguished as a separate DAS component in the global analysis of pump-probe profiles.
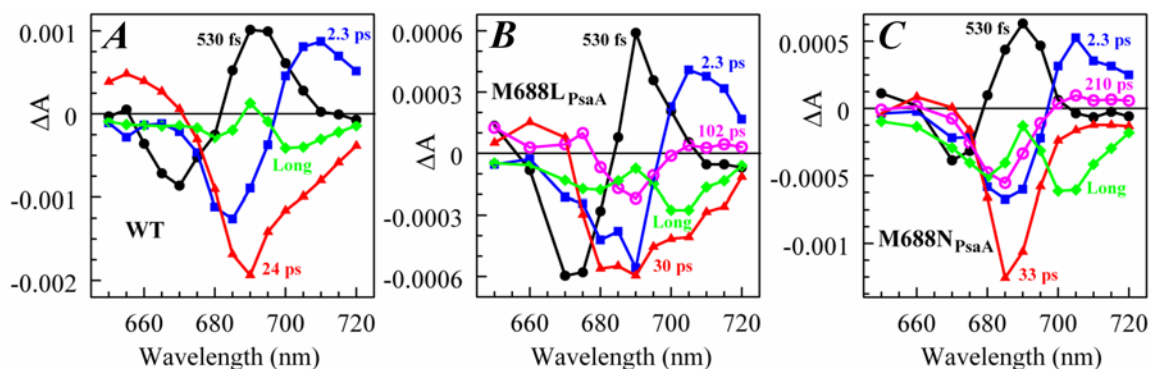


**Fig. 5.5** Decay-associated spectra (DAS) from global analyses of pump-probe data obtained for PS I complexes with open RCs. (A) WT (Savikhin et al. 2000) (B) M688L$_{PsaA}$ mutant shows five distinct components. (C) M688N$_{PsaA}$ mutant shows five distinct components.

## 5.7. Discussions and Analysis

The results described in this work indicate that mutations on the PsaA-branch of PS I markedly alter the kinetics of the first steps of ET as well as the spectral properties of the primary electron acceptor $A_0$, whereas mutations on the PsaB-branch maintain kinetics and spectral properties that are essentially undistinguishable from the WT. The secondary ET $P700^+A_0^-A_1 \rightarrow P700^+A_0A_1^-$ occurs with an intrinsic time of 100–150 ps in the M688L$_{PsaA}$ and M688N$_{PsaA}$ mutants, which is approximately an order of magnitude slower than the secondary ET step in the WT, as determined recently by Savikhin et al. (2001), and it is at least 3 times slower than earlier estimates (Iwaki et al. 1995; White et al. 1996; Brettel and Vos 1999). There are two possible explanations for this effect: (i) in WT PS I complexes ET occurs concurrently along both branches, but the mutation near $A_0$ blocks the ET along the respective RC branch, and the observed ET rate difference in the PsaA- and PsaB-branch mutants is due to different ET rates along PsaA- and PsaB-branches in WT PS I; (ii) ET always occurs primarily along the PsaA-branch and its rate is affected by mutations near $A_0$. In the following we will test these scenarios against the

experimental data in keeping with the assumption that symmetric mutations in the PsaA and PsaB branches cause comparable changes in the properties of the respective $A_0$ Chl.

*Scenario* (i): *ET occurs concurrently along both branches of the RC in the WT, but mutations on the PsaA- and PsaB-branches block transfer along the respective branch.* In this case the two measured $A_0 \rightarrow A_1$ ET rates (13 ps and ~100 ps) characterize ET processes along the PsaA- and PsaB-branches of RC, respectively. This interpretation also implies that both lifetime components must be present in the kinetics of the WT PS I. However, our analysis reveals a single 13 ps component in the kinetics of WT PS I complexes, which can be explained only if at least 80% of ET occurs along PsaA branch. Given the noise level in our data, this argument cannot exclude a scenario in which up to 20% of ET proceeds along the PsaB-branch with an $A_0 \rightarrow A_1$ lifetime of 100–200 ps.

Blocking ET along the PsaA- or PsaB-branch of RC would necessarily lead to the change in the intrinsic charge separation rate. If both branches are active in WT, the observed intrinsic charge separation rate $r_{WT}$ would be equal to a sum of intrinsic charge separation rates along PsaA-branch ($r_A$) and PsaB-branch ($r_B$): $r_{WT} = r_A + r_B$. If the PsaA- or PsaB-branch were blocked in the mutants, the intrinsic charge separation rate would decrease and become $r_B$ and $r_A$, respectively. The ratio $r_A/r_B$ would define the relative yield of ET along the PsaA- and PsaB-branches in the WT. Since our data indicates that at least 80% of ET must occur along PsaA-branch, the $r_A$ must be at least 4 times larger than $r_B$. Therefore, the intrinsic charge separation rates in PsaA- and PsaB-side mutants must differ drastically. According to several studies ET in PS I core complexes is essentially trap-limited (Melkozernov et al. 1997; Beddard 1998; Dorra et al. 1998), or partly trap-limited (Trinkunas and Holzwarth 1996; Holzwarth et al. 1998; Karapetyan et al. 1999; Byrdin et al. 2002). In the case of a trap-limited ET, drastic differences in intrinsic charge separation rate should lead to drastic changes in the effective excitation trapping time, which was not observed in our experiments.

*Scenario* (ii)*: ET occurs primarily along PsaA-branch of the RC in WT and mutated PS I.* The results of our experiments are most consistent with ET proceeding primarily along the PsaA-branch in the WT and mutant PS I. Mutations in the PsaB-branch of the RC have no effect on the effective electronic energy trapping time or on the $A_0^-$ and $A_1^-$

formation kinetics probed at 690 nm and 390 nm. The ($A_0^-$ – $A_0$) spectra for PS I with mutations around $A_0$ on the PsaB-side of the RC are the same as for WT PS I, suggesting that $A_0^-$ is formed on the PsaA-side of the RC. At the same time, mutations around $A_0$ on the PsaA-side of the RC have a dramatic effect on ET kinetics monitored at 390 nm and 690 nm. Moreover, the ($A_0^-$ – $A_0$) spectra for the two PsaA-side mutants differ from each other as well as from the spectrum measured for WT PS I. The latter can be easily explained under the assumption that ET transfer occurs primarily through PsaA-branch of RC: optical properties of the $A_0$ are sensitive to the local protein environment. We also observed a slight change in the effective excitation trapping time. The structure based model of energy transfer in PS I described in (Savikhin et al. 2001) predicts that the observed increase of the effective excitation energy trapping time from 24 ps to 30 ps can be achieved by increasing the intrinsic charge separation time from 1.3 ps to 2.4 ps.

5.8.   Conclusion

The alteration in the ligand to $A_0$ likely causes a change in its redox potential, which alters the kinetic of ET to $A_1$. According to our data, at least 80% of the electrons transferred in these RCs proceed along the PsaA-branch. These results contrast with the finding that ET in PS I from several eukaryotes proceeds with almost equal probability along both branches of the RC.

CHAPTER 6.  PROBING DIELECTRIC PROPERTIES OF THE PS I RC

Nanosecond absorption dynamics at ~685 nm following excitation of PS I from *Synechocystis* sp. PCC 6803 is consistent with electrochromic shift of absorption bands of the Chl *a* pigments in the vicinity of the secondary electron acceptor $A_1$. Based on experimental optical data and structure-based simulations, the effective local dielectric constant has been estimated to be between 3 and 20, which suggests that electron transfer in PS I is accompanied by considerable protein relaxation. Similar effective dielectric constant values have been previously observed for the bacterial photosynthetic reaction center and indicate that protein reorganization leading to effective charge screening may be a necessary structural property of proteins that facilitate the charge transfer function. The data presented here also argue against attributing redmost absorption in PS I to closely spaced antenna Chls (A38 and A39), and suggest that optical transitions of these Chls, along with that of connecting Chl (A40) lay in the range 680–695 nm.

This chapter is based on the following manuscripts:

Dashdorj N., W. Xu, P. Martinsson, P. R. Chitnis and S. Savikhin. 2004. Electrochromic shift of chlorophyll absorption in photosystem I from *Synechocystis* sp. PCC 6803: A probe of optical and dielectric properties around the secondary electron acceptor. *Biophys. J*. 86:3121-3130.

## 6.1.  Electron Transfer Induced Intraprotein Electric Field

The reduction of $A_1$ is complete within a few tens of picoseconds at most in the PS I RC and the Chl $Q_y$ spectral evolution that stems from the preceding primary processes are essentially complete within this time. While the consequent electron transfer from $A_1^-$ to $F_X$ and $F_{A/B}$ do not affect the Chl population directly, the presence of a strong local electric field around these electron transfer cofactors must affect the optical properties of the nearby pigments (Steffen et al. 1994). Savikhin et al. (2001) reported that noticeable optical absorption evolution in the Chl $Q_y$ spectral region spans well into the nanosecond range, and suggested protein relaxation as a possible cause of the observed signal. In this study, we have performed detailed analysis of this effect and propose that the shape and magnitude of these changes are more consistent with an electrochromic shift of the Chl absorption bands which accompanies electron transfer from $A_1$ to $F_X$. Based on the measured data, we are able to estimate the effective dielectric constant deep within PS I. Considerable local reorganization of the interior of the protein must also occur, leading to effective charge screening. These results are consistent with similar measurements of the effective dielectric constant within the bacterial reaction center (Steffen et al. 1994).

## 6.2.  Optical Absorption Evolution in the Chl *a* $Q_y$ Spectral Region

The (P700$^+$– P700) difference spectra measured 200 ps and 3 s after exciting the PS I antenna pigments are shown in Fig. 6.1A (Savikhin et al. 2001). Both spectra were mutually normalized to the same intensities at wavelengths above 700 nm, where we have observed no time evolution in $\Delta A$ after 200 ps. The difference between 200 ps and 3 s (Fig. 6.1C) has a characteristic bimodal shape with a negative band at ~691 and a positive band at ~682 nm. Fig. 6.2 shows time-resolved absorption difference profiles in a 5 μs time window for WT PS I. A 300 ns absorption decay component is built upon the asymptotic signal at 690 nm; this is mirrored by a 300 ns absorption rise components at 680 and 685 nm (but not at 702 nm, where the amplitude of the long time changes in the (P700$^+$– P700) spectrum is very small (Fig. 6.1A)), indicating that the two observed bands in the (3 s − 200 ps) difference spectrum (Fig. 6.1C) originate from the same process.
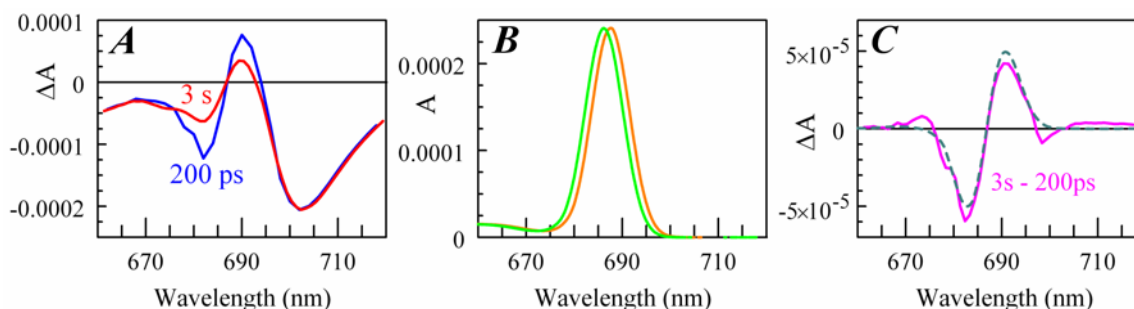
**Fig. 6.1** (A) P700$^+$– P700 absorption difference spectra measured for WT PS I complexes from the cyanobacterium *Synechocystis* sp. PCC 6803 at 200 ps and 3 s. (B) The single-site A$_0$ and connecting Chl *a* absorption spectrum in the case when A$_1$ is reduced and neutral (green) found by fitting $\Delta A$ absorption difference spectra shown in Fig. 1C in assumption that only these two Chls experience electrochromic shift. (C) The difference between the absorption difference spectra measured at 200 ps and at 3s, and the difference between two single-site Chl *a* absorption spectra shown in plane (B).

The consequent electron transfer occurs from A$_1$ to F$_X$ and F$_{A/B}$. None of these cofactors contribute distinctive absorptive bands in the spectral region studied here, and thus cannot be directly responsible for the observed spectral changes. Nevertheless, the measured 300±50 ns kinetics of the change matches the known ~280 ns electron transfer rate from A$_1$ to F$_X$ (van der Est et al. 1994; Brettel 1998; Sakuragi et al. 2002)).



**Fig. 6.2** Absorption difference profiles in 5 μs window for PS I core antenna-reaction center complexes excited at 660 nm and probed at the indicated wavelengths. Noisy curves are experimental difference profiles; smooth profiles are best fits from global analysis of the four profiles using single-exponential kinetics resulting in optimized lifetime of 300 ns.
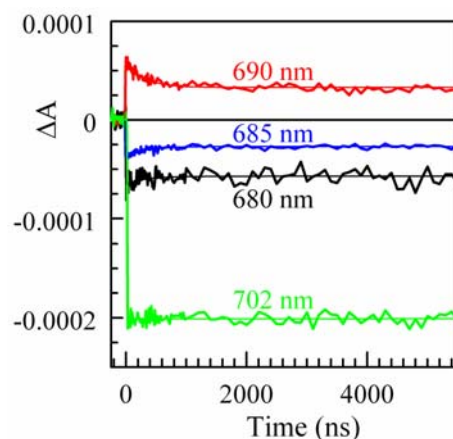
The spectral position, amplitude, and bipolar character of the long time spectral change are consistent with the dynamic shift of Chl absorption band. The transfer of an electron from A$_1$ to F$_X$ will cause drastic changes in the local electric field which will necessarily lead to an electrochromic shift of the optical transitions of the surrounding Chl *a* pigments.

6.3.   Classical Theory of the Electrochromic Effect

The magnitude of the electrochromic shift $\Delta v$ of chromophore absorption band  depends on the changes in permanent dipole moment $\Delta\vec{\mu}$ and polarizability $\Delta\alpha$ that accompany the optical transition, and the local electric field (Liptay 1969; Kakitani et al. 1982):

$$\Delta v = -\frac{1}{hc}\left(|\Delta\vec{\mu}|\ |\vec{E}_{net}|\cos\theta + \frac{1}{2}\Delta\alpha E_{net}^2\right) \tag{6.1}$$

where $\vec{E}_{net}$ is a net electric field at the location of a chromophore due to the presence of an external electric field $\vec{E}$, and $\theta$ is the angle between $\Delta\vec{\mu}$ and $\vec{E}_{net}$; $\Delta\alpha$ is an average scalar polarizability.

The magnitude and direction of the electric field $\vec{E}_e$ at a given atom created by a single electron in vacuum separated by a distance $r$ is given by Coulomb's law:

$$\vec{E}_e = \frac{1}{4\pi\varepsilon_0}\frac{e}{r^2}\hat{r} \tag{6.2}$$

where $\varepsilon_0$ is the permittivity of vacuum, $e$ is the charge of an electron, and $\hat{r}$ is the unit vector from this atom to the charge. Within the protein, the electric field of an electron polarizes the nearby amino acids and the net electric field may be muted (charge screening). The magnitude of this screening depends on the local environment and is defined as the effective static dielectric permittivity (effective dielectric constant) $\varepsilon_{eff}$ (Lockhart and Kim 1992; Steffen et al. 1994):

$$\varepsilon_{eff} = \frac{E_e}{E_{net}} \tag{6.3}$$

The magnitude and the absolute direction of the permanent dipole moment change $\Delta\vec{\mu}$ as well as the value of $\Delta\alpha$ of a chromophore molecule can be found by measuring the classical Stark effect—a shift of the absorption band in homogeneous electrostatic field. Since the effect of the environment on the electric field at the position of the chromophore is not well known, the magnitude of the $|\Delta\vec{\mu}|$ is conventionally measured in units of D/$f$, where $f$ is the local field correction factor which relates to the magnitude of the local field $E_{net}=fE_r$ (Böttcher 1973; Boxer 1993), and $E_r$ is the average macroscopic

electric field in the medium. For monomeric Chl $a$ in PS I it has been found that $|\Delta\vec{\mu}|$=0.5...0.8 (D/$f$) (Rätsep et al. 2000; Zazubovich et al. 2002). A somewhat larger value $|\Delta\vec{\mu}|$=1.02±0.09 D/$f$ was reported for Chl $a$ in a glassy solution (Krawczyk 1991). In the latter work the value of $\Delta\alpha$ for Chl $a$ was also found to be 1.5–4 Å$^3 f^{-2}$, depending on the number of axial ligands. These values of $|\Delta\vec{\mu}|$ and $\Delta\alpha$ suggest that the observed spectral shift of the absorption band is primarily due to $|\Delta\vec{\mu}|$ (linear term in Eq. 6.1): even at the highest observed electric fields ($E_e$=1.76×10$^9$ V/m, Table 1) and the assumption that $\varepsilon_{eff}$=1, the quadratic term in Eq. 6.1, which depends on $\Delta\alpha$, is less than half the size of the linear term. The local correction factor for chromophores in a protein is typically small: $f$ = 1.0...1.5 (Steffen et al. 1994).

The absolute direction of $\Delta\vec{\mu}$ for Chl $a$ has been determined in Stark effect experiments to be almost collinear with the transition dipole moment for the $Q_y$ state has been determined to be along the vector connecting $N_B$ and $N_D$ nitrogen atoms (Lockhart and Boxer 1988; Sener et al. 2002). The angle $\theta$ between the electric field $\vec{E}_e$ and $\Delta\vec{\mu}$ was then computed using the crystal structure (Jordan et al. 2001). Based on these data, the electrochromic shift $\Delta\nu_e$ for both Chls was calculated under the assumption that there is no electrostatic screening effect from the surrounding molecules (Table 1). The observed electrochromic shift $\Delta\nu$ is considerably smaller than $\Delta\nu_e$ and indicates significant electrostatic screening of the electric field.

## 6.4. Electrochromic Shift Calculation in the First Approximation

Since the electric field of an electron is well localized in space (Eq. 6.2), only the Chls nearest to $A_1$ will experience significant electrochromic shifts and need to be considered in the first approximation. According to the X-ray structure of PS I (Jordan et al. 2001), there are two Chls in the immediate vicinity of $A_1$: the primary electron acceptor $A_0$ and the connecting Chl $a$ which is believed to facilitate electronic excitation energy transfer from the PS I antenna to the RC (Fig. 1.6 and Table 1). The direction and magnitude of the electric field $\vec{E}_e$ at the centers of $A_0$ and connecting Chls was calculated using Eq. 6.2

assuming that the extra charge on $A_1^-$ is localized in the geometric center of the atoms contributing to the conjugated π-system (Table 1).

**Table 1** The parameters used to calculate $\varepsilon_{eff}$ based on electrochromic shift of two Chl $a$ molecules that are closest to the secondary electron acceptor $A_1$

| | $A_0$ | Connecting |
|---|---|---|
| $r$ (Å) | 9.0 | 11.2 |
| $E_e$ (V/m) | $1.76 \times 10^9$ | $1.15 \times 10^9$ |
| $\cos(\theta)$ | 0.32...0.34 | 0.47...0.83 |
| $\Delta\nu_e$ (cm$^{-1}$) | −74...−165 | −91...−190 |
| $\Delta\nu$ (cm$^{-1}$) | −13 | −15 |
| $\varepsilon_{eff}$ | 6...13 | |

$r$, distance from $A_1$.
$E_e$, electric field at each of the Chl $a$ due to an electron on $A_1$.
$\theta$, angle between dipole transition moment and electric field vectors.
$\Delta\nu_e$, electrochromic shift expected in absence of screening effect ($\varepsilon_{eff} = 1$).
$\Delta\nu$, an actual shift observed in experiment.

In order to estimate the magnitude of this screening, we modeled the measured electrochromic difference spectrum (Fig. 6.1C) using Eqs. 1 and 3 with two electrochromically shifted Chl $a$ bands representing $A_0$ and the connecting Chl, under the assumption that $\varepsilon_{eff}$ is the same for both molecules. Fig. 6.1C shows the result of the fit of the (3 s − 200 ps) difference spectrum under the assumption that both pigments originally absorb at the same wavelength (~686 nm), when γ=0°, $\Delta\mu$=0.5 D/$f$ and $\Delta\alpha$=1.5 Å$^3f^{-2}$. The best fit was obtained with $\varepsilon_{eff} = 7$, and the corresponding electrochromic shifts for both bands are listed in Table 1. Fig. 1B also shows the net absorption due to these two pigments for the case when $A_1$ is in neutral (green) and reduced states. Reasonable fits could be obtained only with the assumption that the accessory pigment absorption band lies within <5 nm of the $A_0$ absorption band. Uncertainties in $\Delta\mu$ (0.5...1.0 D/$f$), $\Delta\alpha$ (1.5...4 Å$^3f^{-2}$) and γ (−20°...+20°) lead to the range of $\varepsilon_{eff}$ = 6...13.

## 6.5. Electrochromic Shift Simulation

In order to analyze the possible effect on the $\varepsilon_{eff}$ value of including the rest of the pigments, we have calculated $\Delta\nu_e$ magnitudes for all 96 pigments in PS I (Jordan et al. 2001). Each was assumed to have an absorption spectrum similar to the one used for $A_0$, but the maximum position was allowed to change during the fitting procedure (except for $A_0$ and P700, whose absorption maximum positions are known). The screening constant

$\varepsilon_{eff}$ was set to be the same across PS I interior. Together with $\varepsilon_{eff}$, the number of fitting parameters was 95. These free parameters were then varied in order to provide the best fit simultaneously to the steady state absorption spectrum of PS I and the electrochromic shift spectrum shown in Fig. 6.1C. In addition, the parameters were optimized to produce minimal spectral evolution due to the change in the electric field which accompanies electron transfer from $F_X$ to $F_A$, $F_B$ and out from PS I, as such evolution was not observed in our experiments. The latter constraint turned out to dramatically limit the lowest value of $\varepsilon_{eff}$ for which a good fit could be achieved. Perfect fits for all data were obtained with $\varepsilon_{eff}$ = 6.8 (Fig. 6.3A, $\gamma$=0°, $\Delta\alpha$=1.5 Å³$f^{-2}$ and $\Delta\mu$=0.5 D/$f$). In this case, the electrochromic shift signal was clearly dominated by the four pigments nearest to A₁: A₀, connecting pigment, and two antenna pigments (ec-A3, A40, A38 and A39 according to the labeling scheme of (Jordan et al. 2001)).
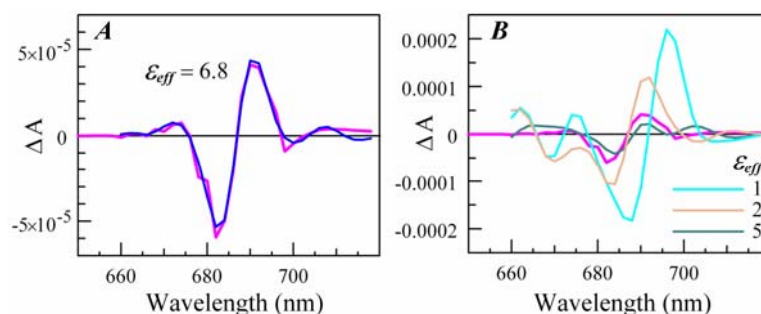


**Fig. 6.3** (A) The measured electrochromic shift signal (fuchsia curve, the same as in Fig. 6.1C), and the best fit (blue curve) to the data obtained in a simulation which includes all antenna pigments ($\gamma$=0°, $\Delta\mu$=0.5 D/$f$, and $\Delta\alpha$=1.5 Å³/$f$). (B) Expected electrochromic shift signals in the case of arbitrary spectral distribution of antenna pigments and $\varepsilon_{eff}$ fixed at 1, 2 and 5.

The absorption maxima positions for these four pigments could be varied within ±3 nm of their optimal positions without affecting the quality of the fit. The spectral positions of the rest of the pigments in PS I were not critical; almost any random spectral distribution could be chosen for these pigments (provided that such a distribution results in the observed steady state absorption spectrum). Uncertainties in $\Delta\mu$ (0.5…1.0 D/$f$), $\Delta\alpha$ (1.5...4 Å³$f^{-2}$) and $\gamma$ (−20°…+20°) lead to the range of $\varepsilon_{eff}$ = 5…15.

Good fits could be also obtained for $\varepsilon_{eff}$ fixed at 2 and 3, but the fitting procedure took considerably longer as progressively more and more pigments had to be arranged in a special manner. If $\varepsilon_{eff} = 3$, both $A_0$ and the connecting pigment each contribute electrochromic shift signals of comparable magnitude and shape as found in the experiment, and the positions of the next closest pigments must be optimized to lower the overall electrochromic signal. We found that for a good fit, the six closest pigments had to be placed within $\pm 3$ nm of their optimal spectral position. When $\varepsilon_{eff} = 2$, each of the four closest to $A_1$ pigments contributes an electrochromic signal which is larger than or comparable to the total signal observed in the experiment. This fit was sensitive to the position of ten closest pigments—the first three pigments had to be within 1 nm of their optimal positions, and the restrictions of the remaining pigments varied progressively from $\pm 2$ nm to $\pm 7$ nm. Any deviation from the optimal spectral arrangement of these pigments would lead to a drastically different electrochromic shift signal. To illustrate that, Fig. 4B shows the expected electrochromic shift signals for $\varepsilon_{eff} = 1$, 2, and 5 (no fitting, $\gamma=0°$, $\Delta\mu=0.5$ D/$f$ and $\Delta\alpha = 1.5$ Å$^3 f^{-2}$) for randomly chosen sets of spectral arrangement of antenna pigments. No fit was possible with $\varepsilon_{eff} \leq 1$. Good fits were also obtained with $\varepsilon_{eff}$ fixed at 8 and 10 ($\gamma=0°$ and $\Delta\mu=0.5$ D/$f$)—in this case more and more pigments had to be arranged in a special manner so that the net electrochromic shift signal would increase and resemble the experimentally measured signal.

PS I function does not require the optimization of pigment arrangement in a way to produce the observed electrochromic shift spectrum. We find it rather improbable that 10 or more pigments near $A_1$ happen to be positioned in a such a rare way as to produce the observed electrochromic shift spectrum, as required in the case of $\varepsilon_{eff} = 2$ or 10. Thus, the most probable value for $\varepsilon_{eff}$ around $A_1$ must be in the range $\varepsilon_{eff} = 3\ldots 8$. Including uncertainties in $\Delta\mu$ (0.5$\ldots$1.0 D/$f$), $\Delta\alpha$ (1.5$\ldots$4 Å$^3 f^{-2}$) and $\gamma$ ($-20°\ldots+20°$) would further widen the range of possible values to $\varepsilon_{eff} = 3\ldots 20$.

## 6.6.   Discussions and Analysis

The value of the effective dielectric constant $\varepsilon_{eff}$ measured in this study is a microscopic parameter and should not be confused with the conventional relative dielectric constant $\varepsilon_r$

which characterizes the average macroscopic electric field. There are three main contributors to the $\varepsilon_{eff}$ in our case: (*i*) the presence of a water shell around the protein, (*ii*) the presence of a protein surrounding the chromophore, and (*iii*) the screening of the electric field due to polarization of the chromophore itself.

In order to estimate the screening effect caused by the water shell, we modeled PS I as an empty spherical cavity within high dielectric constant media ($\varepsilon_r \sim 80$ for water). The size of the cavity and the position of the charge within the cavity were chosen to mimic the size of the PS I complex and the relative position of the secondary electron acceptor $A_1$. According to this model, the presence of a water shell would lead to a decrease of the electric field (screening) at the position of nearby Chl *a* molecules of the order of 10% or less. Comparably small water shell effects have been reported in (Blomberg et al. 1998).

In the case of a medium consisting of similar spherical molecules subjected to a homogeneous external field $E_0$, the average macroscopic electric field $E_r$ within the medium will be $\varepsilon_r$ times smaller than $E_0$ ($E_r = E_0/\varepsilon_r$), and the local electric field $E_{net}$ in the cavity occupied by one of the molecules can be expressed as $E_{net} = fE_r$, where $f = (\varepsilon_r + 2)/3$ (Böttcher 1973; Bublitz and Boxer 1997). Inside a protein $\varepsilon_r$ is low (Rosen 1963; Bone and Pething 1985) and values of $f = 1.0\ldots1.5$ are routinely used (Boxer 1993; Steffen et al. 1994; Rätsep et al. 2000). However, the contribution of the protein medium and the chromophore itself to the value of $f$ is complex in the general case; therefore, in most of the Stark effect studies, the products $f\Delta\mu$ and $f^2\Delta\alpha$ are determined instead. In this paper, the latter values were used in place of $\Delta\mu$ and $\Delta\alpha$, respectively, and Eq. 6.1 should result in a correct prediction of $\Delta\nu$ when $E_r = E_0/\varepsilon_r$ is used in place of $E_{net}$:

$$\Delta\nu = -\frac{1}{hc}\left(|\Delta\vec{\mu}| \left|f\frac{\vec{E}_0}{\varepsilon_r}\right|\cos\theta + \frac{1}{2}\Delta\alpha\left(f\frac{\vec{E}_0}{\varepsilon_r}\right)^2\right) \tag{6.4}$$

In the case of an electric field $E_e$ created by an electron on $A_1$, however, we find that the electrochromic shift is significantly smaller than that predicted by Eq. 6.4 and expected in a conventional Stark experiment when $E_r = E_e/\varepsilon_r$; instead $E_r = E_e/\varepsilon_{eff}$ must be used with $\varepsilon_{eff}$ considerably larger than typical $\varepsilon_r$ values for interior of a protein. This discrepancy

indicates significant local charge screening, lowering the magnitude of the electric field of an electron in the vicinity of $A_1$.

Numerous calculations and experiments have shown that the electrostatic properties of proteins depend strongly on the mobility of charged and polar side chains (Rosen 1963; Bone and Pething 1985; Smith et al. 1993; Simonson 1998; Pitera et al. 2001). The dielectric constant is a direct measure of the polarizability of the protein medium and reflects its relaxation properties in response to a charge perturbation. The high value of $\varepsilon_{eff}$ observed in our experiment suggests that the electron transfer process in PS I is accompanied by a significant reorganization of the surrounding protein structure, leading to effective screening of the electric field produced by the electron. This is consistent with the results obtained in similar experiments on the Stark effect in the bacterial RC (Steffen et al. 1994). According to (Steffen et al. 1994), the high effective dielectric constant may lead to enhanced electronic coupling between reactant and product states by decreasing the tunneling barrier height and increasing orbital overlap. Our results on PS I support this trend and suggest that a high local dielectric constant is perhaps a common attribute of electron transfer sites in proteins. The effective charge screening and associated reorganization energy may also help to stabilize the product state and prevent back transfer (Treutlein et al. 1992).

Recent X-ray structure of PS I (Jordan et al. 2001) reveals 207 water molecules incorporated into this protein structure. Even though the present X-ray resolution is not sufficient to detect all water molecules, it is clear that the concentration of water molecules is especially high in the vicinity of the electron transfer chain formed by secondary electron acceptor $A_1$ and three iron sulfur complexes $F_X$, $F_A$ and $F_B$. We count a total of 17 water molecules within 7 Å of these cofactors, which leads to ~5 times larger local water concentration in this area than the average water concentration in the rest of the protein. The concentration of water molecules is especially high in the area between $A_1$ and $F_X$. The presence of water around electron transfer cofactors may play a crucial role in increasing structural flexibility of surrounding protein side chains (Bone and Pething 1985) necessary for achieving effective dielectric screening. The analysis also reveals that polar and charged side chains exhibit significant clustering in the same area.

The proximity of pigments forming the electron transfer chain in PS I to each other and to connecting chlorophylls may cause noticeable excitonic interactions (Byrdin et al. 2002; Damjanovic et al. 2002; Witt et al. 2002). Excitonic interactions are known to lead to an increase in $\Delta\mu$. It has been shown, for example, that the redmost pigments in PS I absorbing at 714 nm exhibit values of $f\Delta\mu = 2.3\pm0.20$ D, i.e. about four times larger than monomeric Chl $a$ (Rätsep et al. 2000). The latter increase has been attributed to strong excitonic coupling between two or more antenna pigments. The quantitative effect of possible exciton coupling between the pigments surrounding $A_1$ on values and directions of $\Delta\mu$ is not known. However, the inclusion of this effect into our simulation is expected to increase the electrochromic shift effect (and $\varepsilon_{eff}$), unless the angle $\theta$ between $\Delta\vec{\mu}$ and $\vec{E}_{net}$ for the excitonically coupled molecules would be close to 90 degrees.

The electric field of an electron positioned on $A_1$ is well localized in space and thus may serve as a probe of optical properties of the nearby pigments not accessible in conventional optical absorption measurements due to spectral congestion. According to the simulation discussed above, the electrochromic shift of four nearby pigments must account for most of the measured signal. Thus, the absence of electrochromic shift signal at wavelengths above 700 nm argues against assigning A38 and A39 as redmost Chls.

## 6.7. Conclusion

The high effective (local) dielectric constant around electron transfer cofactor $A_1$ in PS I RC reported in this work, along with the previously measured high effective dielectric constant along the active electron transfer branch in bacterial RC (Steffen et al. 1994), indicate that protein reorganization leading to effective charge screening is a necessary structural property of a protein and facilitates effective charge transfer. The electric field of an electron on $A_1$ also serves as an effective probe of optical properties of nearby pigments, which are not otherwise accessible in conventional absorption experiments due to spectral congestion. The measured electrochromic shift signal implies that the Chls A38 and A39 are not the redmost pigments in PS I. The data presented in this work may serve as an important constraint for improving the accuracy of existing and future models of the energy and electron transfer process in this important protein.

CHAPTER 7.  FUTURE DIRECTIONS

There are several areas of investigation which could enhance of our understanding of the functional mechanisms of the two major pigment protein complexes that were studied exclusively in this proposal. Here are some experiments that we have either attempted or contemplated, but which require further refinement or analysis to be complete:

1.  We are in process of submitting a manuscript on long-range triplet-triplet energy transfer from the Chl *a* to β-carotene in the cyt $b_6f$ complex, in which we propose that singlet oxygen molecule acts as energy transfer mediator. One concrete way to test this hypothesis to detect singlet oxygen through its characteristic luminescence around 1270 nm. We are pondering to utilize ultrafast pump-probe spectroscopy, which, if we succeed, would be the first of this kind of experiment.

2.  Preliminary experiments have been carried out on PsaE and/or PsaF subunits deficient mutants of PS I, the results of which indicated that deletion of these subunits influenced excitonic coupling of PS I that is particularly interesting as these subunits are peripheral to the PS I core complex. We will be studying energy and electron transfer dynamics in more detail. These studies would shed more light on the directionality issue of transmembrane electron transfer in PS I, and in addition, in the light of these preliminary results it may provide some insights on the relationship between the function and quartenary structure of PS I.

3.  We will be testing our proposed quenching mechanism of the singlet excited state of the Chl *a* in the cyt $b_6f$ complex via mutating aromatic amino acid residues in the close proximity of the Chl *a*.

4. Based high-resolution crystal structures of the cyt $b_6f$ complex, we are considering to simulate oxygen diffusion through the $b_6f$ complex using molecular dynamics. It is connected to our hypothesis of oxygen-mediated triplet energy transfer that seems very feasible on the basis of experimental data we have (not presented in this proposal).

5. We have performed a set of experiments on *menB* mutants of PS I, in which the secondary electron acceptor $A_1$, a phylloquinone molecule, is replaced with foreign quinone. As continuation of this study, we are considering to study *menB* and *rubA* double deletion mutant, where $A_1$ is completely removed, so that we could study kinetics of the charge recombination and resulting triplet excited state of P700.

APPENDIX I: Detailed Specifications of the Ultrafast Pump-Probe System

**T:S Oscillator**

The self-mode-locked T:S oscillator pumped with 3.5 W at 532 nm using Spectra-Physics Millennia V*s* J diode-pumped continuous-wave (CW) laser. In the T:S oscillator, the titanium-doped sapphire crystal acts as a positive lens for high intensity pulses via the nonlinear optical Kerr effect, leading to spontaneous self-mode-locking. The lasing elements are arranged in folded-Z cavity. The pump beam is focused into the T:S crystal through a dichroic curved mirror (CM3), and two prisms (P1 and P2) are placed in the cavity to provide the negative dispersion required to maintain short pulse duration. A high reflector (M6) is at one end of the cavity, and an output coupler (M7) is at the other end. Output pulses are horizontally polarized. Small portion of the pulse train penetrated through the high reflector is sent to a fast photodiode (PD) to provide a timing signal for the regenerative amplifier.

**Optical Isolator**

The key element in the optical isolator is Electro-Optics Faraday rotator (45˚ rotation angle) that includes a nonlinear magneto-optically active element mounted in a permanent magnet, in which the longitudinal magnetic field induces a circular birefringence that leads to nonreciprocal rotation of polarization. Horizontally polarized pulses from the oscillator are passed through the isolator that is the combination of a double-escape Glan-laser polarizer (GLP), a half waveplate (λ/2) and a Faraday rotator toward the pulse stretcher. On this way, the isolator preserves the polarization of the pulses. After being chirped by the pulse stretcher, the pulses return along the same path. However, this time, the Faraday rotator and half waveplate combination rotates the polarization from horizontal to vertical. Thus, the pulses are reflected by the GLP, sending the vertically polarized and chirped pulses to the regenerative amplifier.

**Pulse Stretcher**

In order to prevent damage due to high peak power to the regenerative amplifier, the pulses were dispersed to ~150 ps duration in a grating pulse stretcher that utilizes a chirp produced with the diffraction grating which send different frequency components on different paths, introducing positive group velocity dispersion (GVD) before the amplification. The full path in the pulse stretcher is folded twice using two mirrors, so that a single grating and a single focusing element can be used in the pulse stretcher. Only the path at the center frequency is shown for simplicity. The pulses from the isolator are directed onto a holographic, gold coated diffraction grating through the top of flat mirror M14. The dispersed beam then travels in the horizontal plane to concave mirror CM12, which reflects it upward just enough to clear the

top of the grating toward flat mirror M13. Mirror M13 sends the beam back to the concave mirror, in such a way that the second diffraction occurs in a slightly dropped plane. Consequently, the group paths run parallel toward M14, where it is reflected at normal incidence, sending the beam backwards along the original path to the isolator. Depicted angles correspond to a center wavelength of 780 nm.

**T:S Regenerative Amplifier**

The regenerative amplifier incorporates Medox Electro-Optics Pockels cell that operates as the fast switch in combination with thin film polarizer within the laser cavity. The Pockels cell is an electro-optic crystal ($KD_2PO_4$) whose birefringence can be modified by applying a DC electric field. A timing signal from the fast PD monitoring the oscillator (Fig. A.1) is divided to produce a 1 kHz synchronized clock that triggers the Q-switch of Clark-MXR ORC-1000 Nd:YAG laser. The 532 nm Nd:YAG pulses with duration of 400 ns create a population inversion in the T:S rod, which is synchronized with injection of a seed pulse via switching a high voltage to the Pockels cell that changes it to a half-wave retarder (full-wave in double-pass). Accordingly, horizontally polarized seed pulse within the cavity remains in the cavity, and is amplified with each pass through the T:S rod. After about eight round trips through the cavity, the pulse is amplified by a factor of $\sim10^6$, and is then ejected via doubling the voltage across the Pockels cell that changes it to $3\lambda/4$ retarder ($3\lambda/2$ in double-pass). To monitor the amplification of the pulse energy within the amplifier cavity, light penetrated through mirror M7 is dispersed into a fast PD. A third pinhole located within the amplifier aids in aligning the seed beam.

**Pulse Compressor**

The holographic, gold-coated diffraction gratings are oriented parallel with angles of incidence and diffraction set to be as indicated that are specified for the center frequency. The incoming beam travels in a single horizontal plane until it reaches the vertical roof mirror, which lowers the plane by 0.5 inch and sends the dispersed beam back through the grating pair. The lowered beam then strikes mirror M17 and directed to the optical parametric amplifier via mirror M18. The distance between the diffraction gratings is adjustable by translating the second grating along the main axis.

**Optical Parametric Amplifier**

The amplified, recompressed pulses were converted in a type I $\beta$-$BaB_2O_4$ (beta barium borate or BBO) optical parametric amplifier (OPA) crystal into infrared signal and idler frequencies in order to have two independently tunable pulse sources, each capable of accessing a very broad wavelength, while maintaining the short pulse duration. The OPA design, after that of Hasson (1997), employed a double-pass configuration, in which OPA process was initiated by continuum seed. The 780 nm fundamental pulse is directed off a high reflector (M3) that transmits 1% of the energy, which is focused into a sapphire plate (SP1) to generate continuum or white light (gray line). An achromatic paraboloidal mirror (M4) collimates the continuum and directs it to a retroreflector (RR) fixed on a translation stage. The reflected portion of the

fundamental pulse is rotated vertical polarization with a half-wave plate ($\lambda/2$), and is then divided into portions using a beamsplitter (BS1). The 9% portion is combined with the horizontally polarized continuum using GLP and is directed into the BBO1 crystal coincident with the continuum seed via a long wavelength passing dichroic mirror (LWP1) as a first stage pump pulse. The transmitted portion of the 90% of the fundamental pulses through BS2 is used to pump the second stage of amplification. The signal and idler outputs of the first stage pass through LWP2, and are then directed to a concave mirror (CM11) that is fixed on a translation stage through a silicon window (SiW), which chirps them due to its large positive dispersion introducing a separation between the signal and idler outputs in time, so that one can selectively amplify one of the outputs by adjusting the second stage timing. Also CM11 collimates the output of the first stage to match the mode size of the second stage pump beam.

**Detection System**

A Gaussian fit to a Kerr-effect cross-correlation profile between 680 nm frequency doubled signal pulses and 700 nm broadband continuum pulses generated in a sapphire plate yielded 98 fs full-width at half-maximum (fwhm), which would correspond to 70 fs fwhm laser pulses if the signal and continuum pulse profiles had identical shapes. Cross-correlations at other wavelengths varied from 100 to 200 fs fwhm. Due to group velocity dispersion in the optics, the timing between pump and probe pulses varied with wavelength, which was calibrated for all combinations of pump and probe wavelengths. The reflected portion of the 90% of the fundamental pulses off BS2 is focused into SP2 to generate the continuum pulses, and used to detect the pump-induced changes in absorbance of the sample in pump-probe experiments. Variable neutral density filters ND1 and ND2 preceding the sapphire plates attenuate the input pulse, so that only a single filament continuum is generated. Typically the signal pulses of the first stage are amplified in the second stage, and are then focused into the BBO frequency-doubling crystal (BBO2) to generate the second-harmonic, which is used as pump pulses in experiments. The pump beam was intersected with the probe beam within the sample, while the reference just passed through the sample. The probe/reference ratio is computed every shot to normalize with respect to intensity fluctuations. Blocking every other pump pulse with synchronized chopper, the pump-induced change in absorbance of the sample was measured. Computer-automated control of monochromator wavelength, pump delay and pump polarization was incorporated into the system. In pump-probe experiments, the second-harmonic of OPA signal pulses served as pump, while the broadband continuum pulses generated in a sapphire crystal are used to detect the pump-induced change in absorbance of the sample. The continuum pulses were split into reference and probe beams; both were focused into the sample, but only the probe beam spatially overlapping with the pump beam within the sample. The reference and probe beams were dispersed in a programmable Oriel MS257 imaging monochromator operated at ~3 nm bandpass, and directed onto separate Hamamatsu S3071 Si PIN photodiodes (5 mm diameter active area). The photodiode signals for every pulse were integrated in Stanford Research Systems SR250 boxcar integrators, and digitized in a

National Instruments MIO-000 16-bit analog-to-digital converter (ADC) computer plug-in module. The pump beam is chopped at 0.5 kHz, and the probe/reference ratio when pumped ($p_{on}$ and $r_{on}$) versus not pumped ($p_{off}$ and $r_{off}$) are computed, which in turn leads to the pump-induced change in absorbance $\Delta A$ that has the following form.

$$\Delta A = -\frac{1}{\ln(10)}\left[\ln\left(\frac{p_{on}}{r_{on}}\right) - \ln\left(\frac{p_{off}}{r_{off}}\right)\right] \tag{A.1}$$

Noise performance was near shot noise-limited; the rms noise in absorption difference measurements was $\sim 3 \times 10^{-5}$ for 1 sec accumulation time. The change in absorbance is measured as a function of both the probe wavelength and the time delay between the pump and probe pulses. The time arrival of the pump pulse was optically delayed via a hollow retroreflector mounted on a computer-controlled translation stage. In anisotropy studies, the pump and probe polarizations were rapidly alternated between parallel and perpendicular using Meadowlark Optics LRC-200-IR1 liquid crystal variable retarder; the time-resolved transient absorption difference at the magic angle ($\Delta A$) and the optical anisotropy ($r$) were then computed from the respective absorbance difference signals ($\Delta A_{\parallel}$ and $\Delta A_{\perp}$, respectively) using the following formulae:

$$\Delta A(t) = \Delta A_{\parallel}(t) + 2\Delta A_{\perp}(t)$$
$$r(t) = \frac{\Delta A_{\parallel}(t) - \Delta A_{\perp}(t)}{\Delta A_{\parallel}(t) + 2\Delta A_{\perp}(t)} \tag{A.2}$$
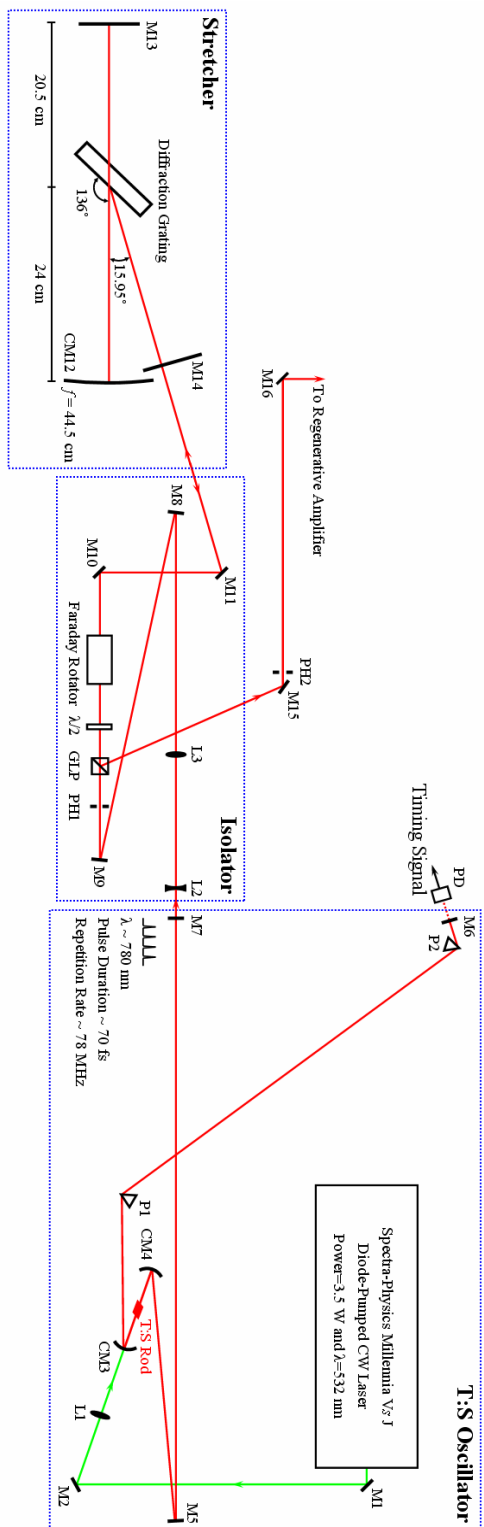
**Fig. A.1** The T:S oscillator, optical isolator and pulse stretcher layout.
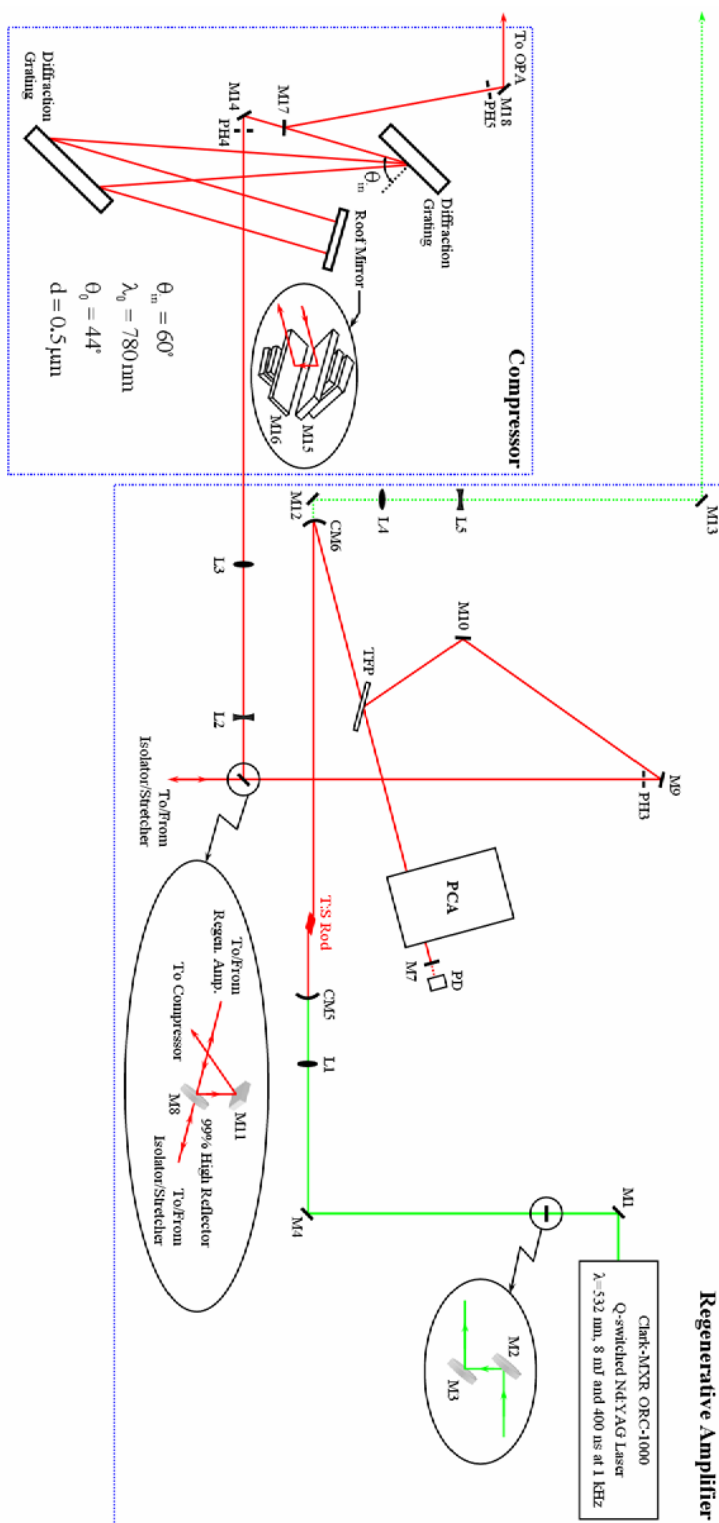
**Fig. A.2** The regenerative amplifier and pulse compressor layout.
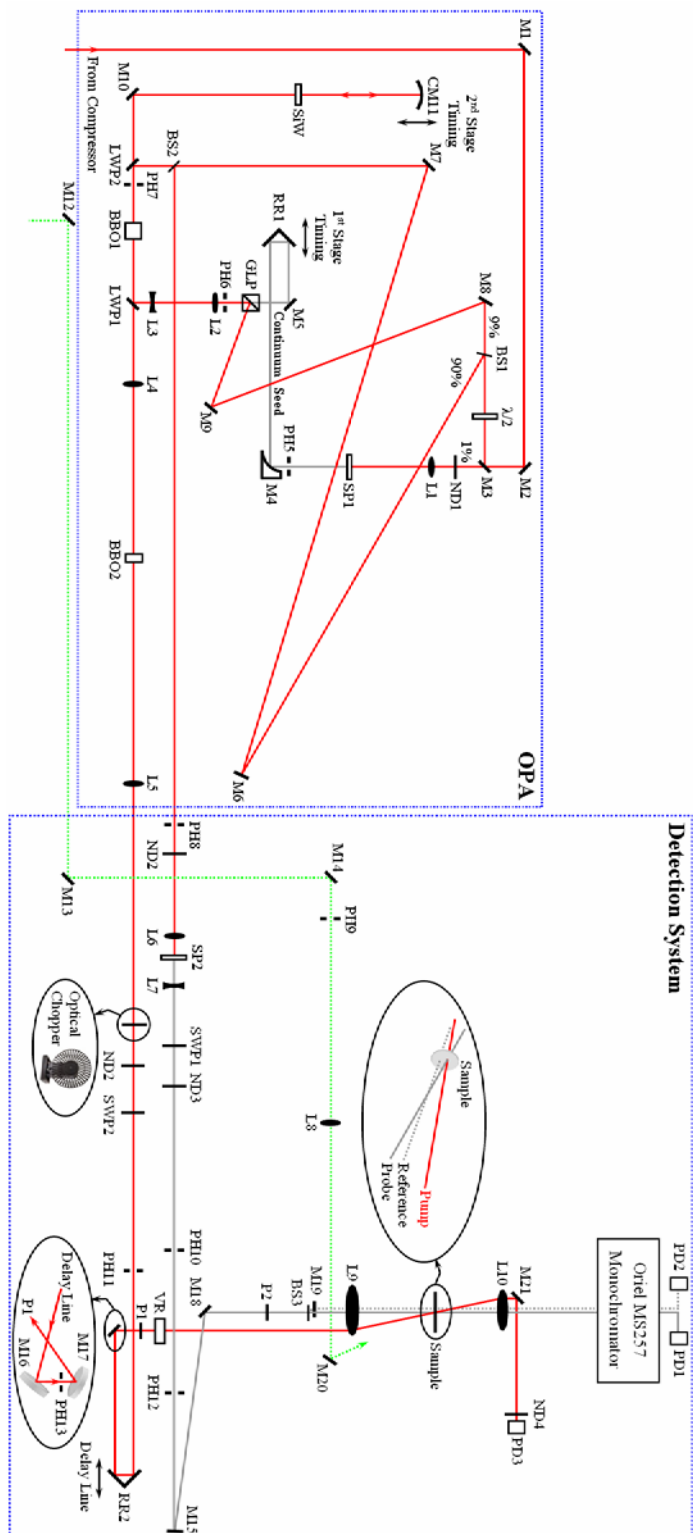
**Fig. A.3** The optical parametric amplifier and detection system layout.

APPENDIX II: Experimental Procedures

## PS I Experimental Procedures

*Sample preparation.* Trimeric PS I complexes were purified from the WT strain of *Synechocystis* sp. PCC 6803 using the method of Sun et al. (1998). The Met688$_{PsaA}$ to Leu688$_{PsaA}$ (M688L$_{PsaA}$) and the Met668$_{PsaB}$ to Leu668$_{PsaB}$ (M668L$_{PsaB}$) mutants were constructed in *Synechocystis* sp. PCC 6803 as described in (Cohen et al. 2004). The Met688$_{PsaA}$ to Asn688$_{PsaA}$ (M688N$_{PsaA}$) and the Met668$_{PsaB}$ to Asn668$_{PsaB}$ (M668N$_{PsaB}$) mutants were constructed similarly.

*Femtosecond pump-probe spectroscopy*. Transient absorption differences $\Delta A$ following optical excitation of the sample were recorded using the femtosecond pump-probe system described in Chapter 2. All PS I samples for ultrafast pump-probe experiments exhibited ~0.3 optical density at the excitation wavelength of 660 nm (the blue edge of the Chl *a* Q$_y$ absorption band) and contained 40 mM sodium ascorbate and 20 μM phenazine methosulfate (PMS) to ensure rapid recovery of the RC. Samples were housed in a spinning cell with 0.7 mm path length; the excitation density was ~1.5 μJ/cm$^2$ (1.5 nJ/pulse, ~300 μm spot size). This yielded an excitation rate of 1 out of every ~1000 Chls. The cell was spinning at ~10 Hz; given the 1 kHz laser repetition rate, successive pulses excited nonoverlapping spots. The pump and probe polarizations were separated by 54.7º, to exclude anisotropy effects in the measured kinetics. Operation in the annihilation-free regime was ensured by control experiments in which the pump power was varied. All experiments were performed at room temperature. In experiments with closed RC, a small fraction of 532 nm, 400 ns pulses from Nd:YAG laser utilized in the femtosecond regenerative amplifier was used to optically close the RC in PS I complexes (Fig. A.2). These pulses preceded pump/probe pulse pair by about 6 μs and were focused into the same spot where the pump and probe pulses intersected within the sample (Fig. A.3). Since comparison between dynamics in PS I with closed and open RC was essential in some experiments, this optical switching automatically ensured amplitude normalization of pump-probe signals accumulated for species with open and closed RC.

*Nanosecond pump-probe spectroscopy*. Excitation pulses were generated using the ultrafast pump-probe system described in Chapter 2. Probe pulses originated in a cavity-dumped dye laser tuned with an intracavity birefringent filter. The cavity dumper timing was derived from sync output pulses of the Pockels cell driver in the pump laser's regenerative amplifier. Variable delays were generated in a modified EG&G GD150 delay line, with its external delay input connected to a PC DAC output. After conversion to 10 ns long TTL pulses using a Tektronix PG501 pulse generator, the GD150 output pulses were directed to the dye laser cavity dumper.

*Steady-state spectroscopy.* PS I samples for steady-state experiments contained 40 mM sodium ascorbate. As shown by Savikhin et al. (2000), samples in experiments conducted in total darkness contained predominantly open RCs; continuous illumination of the sample cell by a 3 V flashlight bulb yielded samples in which the RCs were almost exclusively closed. Steady-state absorption spectra of PS I samples with open and closed RCs were accumulated in a Perkin-Elmer Lambda 3B spectrophotometer modified according to (Savikhin et al. 1999). The (P700$^+$– P700) absorption difference spectra were then obtained by subtracting absorption spectrum of the sample with open RC from that with closed RC.

## Cyt $b_6f$ Complex Experimental Procedures

*Sample preparation.* Purification and crystallization of the cyt $b_6f$ complex is described in detail elsewhere (Zhang et al. 2003; Zhang and Cramer 2004). Cyt $b_6f$ complexes were purified from *M. laminosus* (ML), spinach chloroplasts (Sp) were in enzymatically active dimeric form and contained approximately ~1.2 Chl *a* molecules per cyt *f*, while the purified $b_6f$ complex from *Synechococcus* PCC 7002 contained Chl *a* at a 1.0:1 stoichiometry per cyt *f* and was in enzymatically inactive monomeric form. The stoichiometry of Chl *a* relative to cyt *f* was critical for unambiguous interpretation of the experimental results. To ensure highest sample purity, approximately sixty diffraction quality single crystals of the cyt $b_6f$ complex from ML were dissolved in a buffer containing 30 mM Tris·HCl (pH 7.5), 50 mM NaCl, and 0.05% undecyl-β-D-maltoside. The crystals had a stoichiometry of Chl *a* 1.0:1 relative to cyt *f*, and contained complexes in a functionally active form exhibiting ET rate of ~300 electrons per cyt *f* per second from decyl-plastoquinol to plastocyanin-ferricyanide (Zhang et al. 2003).

*Spectroscopic measurements.* Steady state absorption spectra were measured using a Perkin-Elmer Lambda 3B spectrometer. Transient absorption differences $\Delta A$ following optical excitation of the sample were recorded using the femtosecond pump-probe system described in Chapter 2. All cyt $b_6f$ complex samples were housed in a cell with a 1 mm path length, and exhibited ~0.1 absorbance at the excitation wavelength of 660 nm. Unless otherwise specified, experiments were carried out at room temperature The excitation density was ~100 μJ/cm$^2$ (100 nJ/pulse, ~300 μm spot size). This yielded an excitation rate of 1 out of every ~1000 Chls per excitation pulse. Independence of the measured kinetic profiles on the excitation intensities were ensured by control experiments in which the pump power was varied. Irreversible degradation of the Chl *a* in the cyt $b_6f$ complex and monomeric Chl *a* dissolved in organic solvents in an air-saturated environment was induced by controlled irradiation with light generated using a home-built tunable dye laser. Photodegradation was assayed by the integrated area under the Chl *a* Q$_y$ absorbance band (640–700 nm) as a function of irradiation time.

REFERENCES

Archer M.D. and J. Barber, editors. 2004. Molecular to Global Photosynthesis. River Edge, NJ, USA: Imperial College Press.

Beddard G.S. 1998. Excitations and excitons in photosystem I. *Phil. Trans. R. Soc. London* 356:421-448.

Ben-Shem A., F. Frolow and N. Nelson. 2003. Crystal structure of plant photosystem I. *Nature* 426:630-635.

Berry E.A., M. Guergova-Kuras, L.-S. Huang and A.R. Crofts. 2000. Structure and function of cytochrome *bc* complexes. *Annu. Rev. Biochem.* 69:1005-1075.

Birks J.B. 1970. Photophysics of aromatic molecules. London, UK: Wiley-Interscience.

Blankenship R.E. 2002. Molecular mechanisms of photosynthesis. London, UK: Blackwell Science.

Blomberg M.R.A., P.E.M. Siegbahn and G.T. Babcock. 1998. Modeling electron transfer in biochemistry: a quantum chemical study of charge separation in rhodobacter sphaeroides and photosystem II. *J. Am. Chem. Soc.* 120:8812-8824.

Bodunov E.N. and M.N. Berberan-Santos. 2004. Short-range order effect on resonance energy transfer in rigid solution. *Chem. Phys.* 301:9-14.

Bolton J.R., N. Mataga and G. McLendon, editors. 1991. Electron transfer in inorganic, organic and biological systems. Washington DC, USA: American Chemical Society.

Bone S. and R. Pething. 1985. Dielectric studies of protein hydration and hydration-induced flexibility. *J. Mol. Biol.* 181:323-326.

Böttcher C.J.F. 1973. Theory of Dielectric Polarization. Amsterdam, The Netherlands: Elsevier.

Boudreaux B., F. MacMillan, C. Teutloff, R. Agalarov, F. Gu, S. Grimaldi, R. Bittl, K. Brettel and K. Redding. 2001. Mutations in both sides of the photosystem I reaction center identify the phylloquinone observed by electron paramagnetic resonance spectroscopy. *J. Biol. Chem.* 276:37299-37306.

Bowers P.G. and G. Porter. 1967. Quantum yields of triplet formation in solutions of chlorophyll. *Proc. R. Soc. A* 296:435-441.

Boxer S.G. 1993. Photosynthetic reaction center spectroscopy and electron transfer dynamics in applied electric fields. *In* The Photosynthetic Reaction Center.J. Deisenhofer and Norris J.R., editors, Academic Press, Inc., San Diego, CA, USA. 179-220.

Boyer P.D. 1997. The ATP synthase - a splendid molecular machine. *Annu. Rev. Biochem.* 66:717-749.

Brettel K. 1988. Electron transfer from $A_1^-$ to an iron-sulfur center with $t_{1/2} = 200$ ns at room temperature in photosystem I. Characterization by absorption spectroscopy. *FEBS Lett.* 239:93-98.

Brettel K. 1997. Electron transfer and arrangement of the redox cofactors in photosystem I. *Biochim. Biophys. Acta* 1318:322-373.

Brettel K. 1998. Electron transfer from acceptor $A_1$ to the iron-sulfur cluster in Photosystem I measured with a time resolution of 2 ns. *In* Photosynthesis: Mechanisms and Effects.G. Garab, editor, Kluwer Academic Publishers, Dordrecht, The Netherlands. 611-614.

Brettel K. and W. Leibl. 2001. Electron transfer in photosystem I. *Biochim. Biophys. Acta* 1507:100-114.

Brettel K. and M.H. Vos. 1999. Spectroscopic resolution of the picosecond reduction kinetics of the secondary electron acceptor $A_1$ in photosystem I. *FEBS Lett.* 447:315-317.

Bryant D.A., editor. 1994. The Molecular Biology of Cyanobacteria. Dordrecht, The Netherlands: Kluwer Academic Publishers.

Bublitz G.U. and S.G. Boxer. 1997. Stark spectroscopy: Applications in chemistry, biology and materials science. *Annu. Rev. Phys. Chem.* 48:213-242.

Byrdin M., P. Jordan, N. Krauss, P. Fromme, D. Stehlik and E. Schlodder. 2002. Light harvesting in photosystem I: modeling based on the 2.5-Å structure of photosystem I from *Synechococcus elongatus*. *Biophys. J.* 83:433-457.

Calvin M. 1992. Following the trail of light: A scientific odyssey. Washington, DC, USA: American Chemical Society.

Chitnis P.R. 2001. Photosystem I: Function and physiology. *Annu. Rev. Plant Physiol. Plant Mol. Biol.* 52:593-626.

Cohen R.O., G. Shen, J.H. Golbeck, W. Xu, P.R. Chitnis, A.I. Valieva, A. van der Est, Y. Pushkar and D. Stehlik. 2004. Evidence for asymmetric electron transfer in cyanobacterial photosystem I: Analysis of a methionine-to-leucine mutation of the ligand to the primary electron acceptor $A_0$. *Biochemistry* 43:4741-4754.

Colbow K. 1973. Energy transfer in photosynthesis. *Biochim. Biophys. Acta* 314:320-327.

Cramer W.A. 2004. Ironies in photosynthetic electron transport: a personal perspective. *Photosynth. Res.* 80:293-305.

Cramer W.A. and D.B. Knaff. 1990. Energy transduction in biological membranes: A textbook of bioenergetics. New York, USA: Springer-Verlag.

Cramer W.A., G.M. Soriano, M. Ponamarev, D. Huang, H. Zhang, S.E. Martinez and J.L. Smith. 1996. Some structural aspects and old controversies concerning the cytochrome $b_6f$ complex of oxygenic photosynthesis. *Annu. Rev. Plant Physiol. Plant Mol. Biol.* 47:477-508.

Cramer W.A., H. Zhang, J. Yan, G. Kurisu and J.L. Smith. 2004. Evolution of photosynthesis: Time-independent structure of the cytochrome $b_6f$ complex of oxygenic photosynthesis. *Biochemistry* 43:5921-5929.

Damjanovic A., H.M. Vaswani, P. Fromme and G.R. Fleming. 2002. Chlorophyll excitations in photosystem I of *Synechococcus elongatus*. *J. Phys. Chem. B* 106:10251-10262.

Dashdorj N., W. Xu, R.O. Cohen, J.H. Golbeck and S. Savikhin. 2005a. Asymmetric electron transfer in cyanobacterial photosystem I: Charge separation and secondary electron transfer dynamics of mutations near the primary electron acceptor $A_0$. *Biophys. J.* 88:1238-1249.

Dashdorj N., W. Xu, R.O. Cohen, J.H. Golbeck and S. Savikhin. 2005b. Probing the active electron transfer branch in the photosystem I reaction center from *Synechocystis* sp. PCC 6803. *In* Photosynthesis: Fundamental Aspects to Global

Perspectives.A. van der Est and Bruce D., editors, ACG Publishing, Lawrence, KS, USA. 30-33.

Dashdorj N., W. Xu, P. Martinsson, P.R. Chitnis and S. Savikhin. 2004. Electrochromic shift of chlorophyll absorption in photosystem I from *Synechocystis* sp. PCC 6803: A probe of optical and dielectric properties around the secondary electron acceptor. *Biophys. J.* 86:3121-3130.

Dashdorj N., H. Zhang, H. Kim, J. Yan, W.A. Cramer and S. Savikhin. 2005c. The single chlorophyll *a* molecule in the cytochrome $b_6f$ complex: Unusual optical properties protect the complex against singlet oxygen. *Biophys. J.* 88:1-10.

Dashdorj N., H. Zhang, H. Kim, J. Yan, W.A. Cramer and S. Savikhin. 2005d. Unusual optical properties of the monomeric chlorophyll *a* in the cytochrome $b_6f$ complex of oxygenic photosynthesis. *In* Photosynthesis: Fundamental Aspects to Global Perspectives.A. van der Est and Bruce D., editors, ACG Publishing, Lawrence, KS, USA. 451-453.

DeFelippis M.R., C.P. Murthy, F. Broitman, D. Weinraub, M. Faraggi and M.H. Klapper. 1991. Electrochemical properties of tyrosine phenoxy and tryptophan indolyl radicals in peptides and amino acid analogs. *J. Phys. Chem.* 95:3416 - 3419.

DeFelippis M.R., C.P. Murthy, M. Faraggi and M.H. Klapper. 1989. Pulse radiolytic measurement of redox potentials: the tyrosine and tryptophan radicals. *Biochemistry* 28:4847-4853.

Dexter D.L. 1953. A theory of sensitized luminescence in solids. *J. Chem. Phys.* 21:836-850.

Diner B.A. and F. Rappaport. 2002. Structure, dynamics and energetics of the primary photochemistry of photosystem II of oxygenic photosynthesis. *Annu. Rev. Plant Biol.* 53:551-580.

Dorra D., P. Fromme, N.V. Karapetyan and A.R. Holzwarth. 1998. Fluorescence kinetics of photosystem I: Multiple fluorescence components. *In* Photosynthesis: Mechanisms and Effects.G. Garab, editor, Kluwer Academic Publishers, Dordrecht, The Netherlands. 587-590.

Fairclough W.V., M.C.W. Evans, S. Purton, S. Jones, S.E.J. Rigby and P. Heathcote. 2001. Site-directed mutagenesis of PsaA:M684 in *Chlamydomonas reinhardtii. In* PS2001 proceedings: 12th International Congress on Photosynthesis, CSIRO Publishers, Melbourne, Australia.

Ferreira K.N., T.M. Iverson, K. Maghlaoui, J. Barber and S. Iwata. 2004. Architecture of the photosynthetic oxygen-evolving center. *Science* 303:1831-1838.

Foote C.S. 1976. Photosensitized oxidation and singlet oxidation: consequences in biological systems. *In* Free Radicals in Biology.W.A. Pryor, editor, Academic Press, New York. 85-133.

Förster T. 1948. Zwischemolekulare energiewanderung und fluoreszenz. *Ann. Physik.* 2:55-67.

Förster T. 1965. Delocalized excitation and excitation transfer. *In* Modern Quantum Chemistry.O. Sinanoslu, editor, Academic Press, New York, USA. 93-137.

Fujimori E. and R. Livingston. 1957. Interactions of chlorophyll in its triplet state with oxygen, carotene, etc. *Nature* 180:1036-1038.

Gibbons C., M.G. Montgomery, A.G.W. Leslie and J.E. Walker. 2000. The structure of the central stalk in bovine $F_1$-ATPase at 2.4 Å resolution. *Nature Struct. Biol.* 7:1055-1061.

Girvin M.E. and W.A. Cramer. 1984. A redox study of the electron transport pathway responsible for generation of the slow electrochromic phase in chloroplasts. *Biochim. Biophys. Acta* 767:29-38.

Golbeck J., W. Xu, B. Zybailov, A. van der Est, J. Pushkar, S. Zech, D. Stehlik and P.R. Chitnis. 2001. Electron transfer through the quinone acceptor in cyanobacterial Photosystem I. *In* PS2001 proceedings: 12th International Congress on Photosynthesis, CSIRO Publishing, Melbourne, Australia.

Goldsmith J.O., B. King and S.G. Boxer. 1996. Mg coordination by amino acid side chains is not required for assembly and function of the special pair in bacterial photosynthetic reaction centers. *Biochemistry* 35:2421-2428.

Gottfried K. and T.-M. Yan. 2004. Quantum mechanics: Fundamentals. New York, USA: Springer-Verlag. 620 p.

Graham L.E. and L.W. Wilcox. 2000. Algae. Upper Saddle River, NJ, USA: Prentice-Hall.

Gray H.B. and J.R. Winkler. 2003. Electron tunneling through proteins. *Q. Rev. Biophys.* 36:341-372.

Guergova-Kuras M., B. Boudreaux, A. Joliot, P. Joliot and K. Redding. 2001. Evidence for two active branches for electron transfer in photosystem I. *Proc. Natl. Acad. Sci. U.S.A* 98:4437-4442.

Hanson L.K. 1990. Molecular orbital theory of monomer pigments. *In* Chlorophylls.H. Scheer, editor, CRC Press, Boca Raton. 993-1014.

Harriman A. 1987. Further comments on the redox potentials of tryptophan and tyrosine. *J. Phys. Chem.* 91:6102-6104.

Hasson K.C. 1997. Time-resolved studies of the protein bacteriorhodopsin using femtosecond laser pulses [Ph.D.]. Cambridge, MA: Harvard University. 169 p.

Hastings G., F.A.M. Kleinherenbrink, S. Lin, T.J. McHugh and R.E. Blankenship. 1994. Observation of the reduction and reoxidation of the primary electron acceptor in photosystem I. *Biochemistry* 33:3193-3200.

Hirschfelder J.O. and W.J. Meath. 1967. The nature of intermolecular forces. *In* Intermolecular Forces.J.O. Hirschfelder, editor, Wiley-Interscience, New York, USA. 3-106.

Holzwarth A.R., D. Dorra, M.G. Müller and N.V. Karapetyan. 1998. Structure-function relationships and excitation dynamics in photosystem I. *In* Photosynthesis: Mechanism and Effects.G. Garab, editor, Kluwer Academic Publishers, Dordrecht, The Netherlands. 497-502.

Hopfield J.J. 1974. Electron transfer between biological molecules by thermally activated tunneling. *Proc. Natl. Acad. Sci. U.S.A* 71:3640-3644.

Huang D., R.M. Everly, R.H. Cheng, J.B. Heymann, H. Schägger, V. Sled, T. Ohnishi, T.S. Baker and W.A. Cramer. 1994. Characterization of the chloroplast cytochrome $b_6f$ complex as a structural and functional dimer. *Biochemistry* 33:4401-4409.

Iwaki M., S. Kumazaki, K. Yoshihara, T. Erabi and S. Itoh. 1995. $\Delta G^0$ dependence of the rate constant of $P700^+A_0^- \rightarrow P700^+Q^-$ reaction in the quinone-reconstituted

photosystem I reaction center. *In* Photosynthesis: From Light to Biosphere.P. Mathis, editor, Kluwer Academic Publishers, Dordrecht, The Netherlands. 147-150.

Iwata S. and J. Barber. 2004. Structure of photosystem II and molecular architecture of the oxygen evolving centre. *Curr. Opin. Struc. Biol.* 14:447-453.

Iwata S., J.W. Lee, K. Okada, J.K. Lee, M. Iwata, B. Rasmussen, T.A. Link, S. Ramaswamy and B.K. Jap. 1998. Complete structure of the 11-subunit bovine mitochondrial cytochrome $bc_1$ complex. *Science* 281:64-71.

Jen J.J. and G. MacKinney. 1970. On the photodecomposition of chlorophyll *in vitro* - I. Reaction rates. *Photochem. Photobiol.* 11:297-302.

Joliot P. and A. Joliot. 1994. Mechanism of electron transfer in the cytochrome *b/f* complex of algae: Evidence for a semiquinone cycle. *Proc. Natl. Acad. Sci. U.S.A* 91:1034-1038.

Joliot P. and A. Joliot. 1999. In vivo analysis of the electron transfer within photosystem I: Are the two phylloquinones involved? *Biochemistry* 38:11130-11136.

Jones W.E. and M.A. Fox. 1994. Determination of excited-state redox potentials by phase-modulated voltammetry. *J. Phys. Chem.* 98:5095-5099.

Jordan P., P. Fromme, H.T. Witt, O. Klukas, W. Saenger and N. Krauss. 2001. Three-dimensional structure of cyanobacterial photosystem I at 2.5 Å resolution. *Nature* 411:909-917.

Jortner J. 1976. Temperature dependent activation energy for electron transfer between biological molecules. *J. Chem. Phys.* 64:4860-4867.

Jovanovic S.V., S. Steenken and M.G. Simic. 1991. Kinetics and energetics of one-electron-transfer reactions involving tryptophan neutral and cation radicals. *J. Phys. Chem.* 95:684-687.

Junge W., H. Lill and S. Engelbrecht. 1997. ATP synthase: An electrochemical transducer with rotatory mechanics. *Trends Biochem. Sci.* 22:420-423.

Kakitani T., B. Honig and A.R. Crofts. 1982. Theoretical studies of the electrochromic response of carotenoids in photosynthetic membranes. *Biophys. J.* 39:57.

Kamiya N. and J.-R. Shen. 2003. Crystal structure of oxygen-evolving photosystem II from *Thermosynechococcus vulcanus* at 3.7-Å resolution. *Proc. Natl. Acad. Sci. U.S.A* 100:98-103.

Karapetyan N.V., A.R. Holzwarth and M. Rögner. 1999. The photosystem I trimer of cyanobacteria: Molecular organization, excitation dynamics and physiological significance. *FEBS Lett.* 460:395-400.

Karen A., N. Ikeda, N. Mataga and F. Tanaka. 1983. Picosecond laser photolysis studies of fluorescence quenching mechanisms of flavin: a direct observation of indole-flavin singlet charge transfer state formation in solutions and flavoenzymes. *Photochem. Photobiol.* 37:495-502.

Karplus P.A., M.J. Daniels and J.R. Herriott. 1991. Atomic structure of ferredoxin-$NADP^+$ reductase: Prototype for a structurally novel flavoenzyme family. *Science* 251:60-66.

Kramer D.M. and A.R. Crofts. 1993. The concerted reduction of the high- and low-potential chains of the *bf* complex by plastoquinol. *Biochim. Biophys. Acta* 1183:72-84.

Krawczyk S. 1991. Electrochromism of chlorophyll a monomer and special pair dimer. *Biochim. Biophys. Acta* 1056:64-70.

Krinsky N.I. 1979. Carotenoid protection against oxidation. *Pure Appl. Chem.* 51:649-660.

Kühlbrandt W. 2003. Dual approach to a light problem. *Nature* 426:399-400.

Kurisu G., M. Kusunoki, E. Katoh, T. Yamazaki, K. Teshima, Y. Onda, Y. Kimata-Ariga and T. Hase. 2001. Structure of the electron transfer complex between ferredoxin and ferredoxin-$NADP^+$ reductase. *Nature* 8:117-121.

Kurisu G., H. Zhang, J.L. Smith and W.A. Cramer. 2003. Structure of the cytochrome $b_6f$ complex of oxygenic photosynthesis: tuning the cavity. *Science* 302:1009-1014.

Li Y.-F., W. Zhou, R.E. Blankenship and J.P. Allen. 1997. Crystal structure of the bacteriochlorophyll *a* protein from *Chlorobium tepidum*. *J. Mol. Biol.* 271:456-471.

Liptay W. 1969. Electrochromism and solvatochromism. *Angew. Chem. Internat. Edit.* 8:177-188.

Lockhart D.J. and S.G. Boxer. 1988. Stark effect spectroscopy of *Rhodobacter sphaeroides* and *Rhodopseudomonas viridis* reaction centers. *Proc. Natl. Acad. Sci. U.S.A* 85:107-111.

Lockhart D.J. and P.S. Kim. 1992. Internal Stark effect measurement of the electric field at the amino terminus of an α helix. *Science* 257:947-951.

Lüneberg J., P. Fromme, P. Jekow and E. Schlodder. 1994. Spectroscopic characterization of PS I core complexes from thermophilic *Synechococcus* sp.: Identical reoxidation kinetics of $A_1^-$ before and after removal of the iron-sulfur-clusters $F_A$ and $F_B$. *FEBS Lett.* 338:197-202.

Marcus R.A. and N. Sutin. 1985. Electron transfers in chemistry and biology. *Biochim. Biophys. Acta* 811:265-322.

Mataga N., H. Chosrowjan, Y. Shibata, F. Tanaka, Y. Nishina and K. Shiga. 2000. Dynamics and mechanisms of ultrafast fluorescence quenching reactions of flavin chromophores in protein nanospace. *J. Phys. Chem. B* 104:10667-10677.

Melkozernov A.N., H. Su, S. Lin, S. Bingham, A.N. Webber and R.E. Blankenship. 1997. Specific mutations near the primary donor in photosystem I from *Chlamydomonas reinhardtii* alters trapping time and spectroscopic properties of P700. *Biochemistry* 36:2898-2907.

Miller J.R., J.V. Beitz and R.K. Huddleston. 1984. Effect of free energy on rates of electron transfer between molecules. *J. Am. Chem. Soc.* 106:5057-5068.

Mitchell P. 1975. The protonmotive Q cycle: A general formulation. *FEBS Lett.* 52:137-139.

Moser C.C., J.M. Keske, K. Warncke, R.S. Farid and P.L. Dutton. 1992. Nature of biological electron transfer. *Nature* 355:796-802.

Moser C.C., C.C. Page, R. Farid and P.L. Dutton. 1995. Biological Electron Transfer. *J. Bioenerg. Biomembr.* 27:263-274.

Muhiuddin I.P., P. Heathcote, S. Carter, S. Purton, S.E.J. Rigby and M.C.W. Evans. 2001. Evidence from time resolved studies of the $P700^+/A_1^-$ radical pair for photosynthetic electron transfer on both the PsaA and PsaB branches of the Photosystem I reaction centre. *FEBS Lett.* 503:56-60.

Oda N., K. Tsuji and A. Ichimura. 2001. Voltammetric measurements of redox potentials of photo-excited species. *Anal. Science* 17:i375-i378.

Page C.C., C.C. Moser, X. Chen and P.L. Dutton. 1999. Natural engineering principles of electron tunneling in biological oxidation-reduction. *Nature* 402:47-52.

Page C.C., C.C. Moser and P.L. Dutton. 2003. Mechanism for electron transfer within and between proteins. *Curr. Opin. Chem. Biol.* 7:551-556.

Peterman E.J.G., S. Wenk, T. Pullerits, L.-O. Pålsson, R. van Grondelle, J.P. Dekker, M. Rögner and H. van Amerongen. 1998. Fluorescence and absorption spectroscopy of the weakly fluorescent chlorophyll a in cytochrome $b_6f$ of *Synechocystis* PCC6803. *Biophys. J.* 75:389-398.

Pierre Y., C. Breyton, D. Kramer and J.-L. Popot. 1995. Purification and characterization of the cytochrome $b_6f$ complex from *Chlamydomonas reinhardtii*. *J. Biol. Chem.* 270:29342-29349.

Pierre Y., C. Breyton, Y. Lemoine, B. Robert, C. Vernotte and J.-L. Popot. 1997. On the presence and role of a molecule of chlorophyll *a* in the cytochrome $b_6f$ complex. *J. Biol. Chem.* 272:21901-21908.

Pitera J.W., M. Falta and W.F. van Gunsteren. 2001. Dielectric properties of proteins from simulations: the effect of solvent, ligands, pH, and temperature. *Biophys. J.* 80:2546-2555.

Rastogi V.K. and M.E. Girvin. 1999. Structural changes linked to proton translocation by subunit *c* of the ATP synthase. *Nature* 402:263-268.

Rätsep M., T.W. Johnson, P.R. Chitnis and G.J. Small. 2000. The red-absorbing chlorophyll *a* antenna states of photosystem I: A hole-burning study of *Synechocystis* sp. PCC 6803 and its mutants. *J. Phys. Chem. B* 104:836-847.

Redinbo M.R., D. Cascio, M.K. Choukair, D. Rice, S. Merchant and T.O. Yeates. 1993. The 1.5 Å crystal structure of plastocyanin from the green alga *Chlamydomonas reinhardtii*. *Biochemistry* 32:10560-10567.

Renger G. 1992. Energy transfer and trapping in photosystem II. *In* The Photosystems: Structure, Function and Molecular Biology.J. Barber, editor, Elsevier, Amsterdam, The Netherlands. 45-99.

Rosen D. 1963. Dielectric properties of protein powders with adsorbed water. *Trans. Faraday Soc.* 59:2178-2191.

Sakuragi Y., B. Zybailov, G. Shen, A.D. Jones, P.R. Chitnis, A. van der Est, R. Bittl, S. Zech, D. Stehlik, J.H. Golbeck and D.A. Bryant. 2002. Insertional inactivation of the menG gene, encoding 2-phytyl-1,4-naphthoquinone methyltransferase of Synechocystis sp. PCC 6803, results in the incorporation of 2-phytyl-1,4-naphthoquinone into the A1 site and alteration of the equilibrium constant between A1 and FX in Photosystem I. *Biochemistry* 41:394-405.

Savikhin S. 2005. Ultrafast optical spectroscopy of photosystem I. *In* Photosystem I: The Plastocyanin-Ferredoxin Oxidoreductase in Photosynthesis.J.H. Golbeck, editor, Kluwer Academic Publishers, Dordrecht, The Netherlands. in press.

Savikhin S. and W.S. Struve. 1994. Femtosecond pump-probe spectroscopy of bacteriochlorophyll *a* monomers in solution. *Biophys. J.* 67:2002-2007.

Savikhin S., W. Xu, P.R. Chitnis and W.S. Struve. 2000. Ultrafast primary processes in PS I from *Synechocystis* sp. PCC 6803: Roles of P700 and $A_0$. *Biophys. J.* 79:1573-1586.

Savikhin S., W. Xu, P. Martinsson, P.R. Chitnis and W.S. Struve. 2001. Kinetics of charge separation and $A_0^- \rightarrow A_1$ electron transfer in photosystem I reaction centers. *Biochemistry* 40:9282-9290.

Savikhin S., W. Xu, V. Soukoulis, P.R. Chitnis and W.S. Struve. 1999. Ultrafast primary processes in photosystem I of the cyanobacterium *Synechocystis* sp. PCC 6803. *Biophys. J.* 76:3278-3288.

Savikhin S., W. Zhou, R.E. Blankenship and W.S. Struve. 1994. Femtosecond energy transfer and spectral equilibration in bacteriochlorophyll a—protein antenna trimers from the green bacterium *Chlorobium tepidum. Biophys. J.* 66:110-113.

Schödel R., K.-D. Irrgang, J. Voigt and G. Renger. 1998. Rate of carotenoid triplet formation in solubilized light-harvesting complex II (LHCII) from spinach. *Biophys. J.* 75:3143-3153.

Seely G.R. and J.S. Connolly. 1986. Fluorescence of photosynthetic pigments in vitro. *In* Light Emission by Plants and Bacteria.Govindjee, Amesz J. and Fork D.C., editors, Academic Press, New York. 99-133.

Sener M.K., D. Lu, T. Ritz, S. Park, P. Fomme and K. Schulten. 2002. Robustness and optimality of light harvesting in cyanobacterial photosystem I. *J. Phys. Chem. B* 106:7948-7960.

Senior A.E., S. Nadanaciva and J. Weber. 2002. The molecular mechanism of ATP synthesis by $F_1F_0$-ATP synthase. *Biochim. Biophys. Acta* 1553:188-211.

Siefermann-Harms D. 1987. The light-harvesting and protective functions of carotenoids in photosynthetic membranes. *Physiol. Plantarum* 69:561-568.

Simonson T. 1998. Dielectric constant of cytochrome *c* from simulations in a water droplet including all electrostatic interactions. *J. Am. Chem. Soc.* 120:4875-4876.

Smith P.E., R.M. Brunne, A.E. Mark and W.F. van Gunsteren. 1993. Dielectric properties of trypsin inhibitor and lysozyme calculated from molecular dynamics simulations. *J. Phys. Chem.* 97:2009-2014.

Steffen M.A., K. Lao and S.G. Boxer. 1994. Dielectric asymmetry in the photosynthetic reaction center. *Science* 264:810-816.

Stock D., A.G.W. Leslie and J.E. Walker. 1999. Molecular architecture of the rotary motor in ATP synthase. *Science* 286:1700-1705.

Stroebel D., Y. Choquet, J.-L. Popot and D. Picot. 2003. An atypical haem in the cytochrome $b_6f$ complex. *Nature* 426:413-418.

Struve W.S. 1995. Theory of electronic energy transfer. *In* Anoxygenic photosynthetic bacteria.R.E. Blankenship, Madigan M.T. and Bauer C.E., editors, Kluwer Academic Publishers, Dordrecht, the Netherlands. 297-313.

Sun J., A. Ke, P. Jin, V.P. Chitnis and P.R. Chitnis. 1998. Isolation and functional study of photosystem I subunits in the cyanobacterium *Synechocystis* sp. PCC 6803. *Meth. Enzymol.* 297:124-139.

Treutlein H., K. Schulten, A.T. Brünger, M. Karplus, J. Deisenhofer and H. Michel. 1992. Chromophore-protein interactions and the function of the photosynthetic

reaction center: A molecular dynamics study. *Proc. Natl. Acad. Sci. U.S.A* 89:75-79.

Trinkunas G. and A.R. Holzwarth. 1996. Kinetic modeling of exciton migration in photosynthetic systems. 3. Application of genetic algorithms to simulations of excitation dynamics in three dimensional photosystem core reaction center complexes. *Biophys. J.* 71:351-364.

Trumpower B.L. 1990. The protonmotive Q cycle. Energy transduction by coupling of proton translocation to electron transfer by the cytochrome $bc_1$ complex. *J. Biol. Chem.* 265:11409-11412.

van der Est A., C. Bock, J. Golbeck, K. Brettel, P. Setif and D. Stehlik. 1994. Electron transfer from the acceptor A1 to the iron-sulfur centers in photosystem I as studied by transient EPR spectroscopy. *Biochemistry* 33:11789-97.

van Grondelle R. 1985. Excitation energy transfer, trapping and annihilation in photosynthetic systems. *Biochim. Biophys. Acta* 811:147-195.

van Grondelle R.J., J.P. Dekker, T. Gillbro and V. Sundstrom. 1994. Energy trapping and transfer in photosynthesis. *Biochim. Biophys. Acta* 1187:1-65.

Visser A.J.W.G., A. van Hoek, T. Kulinski and J.L. Gall. 1987. Time-resolved fluorescence studies of flavodoxin. Demonstration of picosecond fluorescence lifetimes of FMN in *Desulfovibrio* flavodoxins. *FEBS Lett.* 224:406-410.

Watanabe T. and M. Kobayashi. 1990. Electrochemistry of chlorophylls. *In* Chlorophylls.H. Scheer, editor, CRC Press, Boca Raton. 287-315.

White N.T.H., G.S. Beddard, J.R.G. Thorne, T.M. Feehan, T.E. Keyes and P. Heathcote. 1996. Primary charge separation and energy transfer in the photosystem I reaction center of higher plants. *J. Phys. Chem.* 100:12086-12099.

Witt H., E. Schlodder, C. Teutloff, J. Niklas, E. Bordignon, D. Carbonera, S. Kohler, A. Labahn and W. Lubitz. 2002. Hydrogen bonding to P700: Site-directed mutagenesis of threonine A739 of photosystem I in *Chlamidomonas reinhardtii*. *Biochemistry* 41:8557-8569.

Xia D., C.-A. Yu, H. Kim, J.-Z. Xia, A.M. Kachurin, L. Zhang, L. Yu and J. Deisenhofer. 1997. Crystal structure of the cytochrome $bc_1$ complex from bovine heart mitochondria. *Science* 277:60-66.

Xu W., P.R. Chitnis, A. Valieva, A. van der Est, K. Brettel, M. Guergova-Kuras, Y.N. Pushkar, S.G. Zech, D. Stehlik, G. Shen, B. Zybailov and J.H. Golbeck. 2003a. Electron transfer in cyanobacterial photosystem I: II. Determination of forward electron transfer rates of site-directed mutants in a putative electron transfer pathway from $A_0$ through $A_1$ to $F_X$. *J. Biol. Chem.* 278:27876-27887.

Xu W., P.R. Chitnis, A. Valieva, A. van der Est, Y.N. Pushkar, M. Krzystyniak, C. Teutloff, S.G. Zech, R. Bittl, D. Stehlik, B. Zybailov, G. Shen and J.H. Golbeck. 2003b. Electron transfer in cyanobacterial photosystem I: I. Physiological and spectroscopic characterization of site-directed mutants in a putative electron transfer pathway from $A_0$ through $A_1$ to $F_X$. *J. Biol. Chem.* 278:27864-27875.

Yoshida M., E. Muneyuki and T. Hisabori. 2001. ATP synthase-a marvellous rotary engine of the cell. *Nature Rev. Mol. Cell Biol.* 2:669-677.

Zazubovich V., S. Matsuzaki, T.W. Johnson, J.M. Hayes, P.R. Chitnis and G.J. Small. 2002. Red antenna states of photosystem I from cyanobacterium *Synechococcus elongatus*: a spectral hole burning study. *Chem. Phys.* 275:47-59.

Zhang H. and W.A. Cramer. 2004. Purification and crystallization of the cytochrome $b_6f$ complex in oxygenic photosynthesis. *In* Photosynthesis Research Protocols.R. Carpentier, editor, Humana Press, Totowa, NJ. 67-78.

Zhang H., D. Huang and W.A. Cramer. 1999. Stoichiometrically bound β-carotene in the cytochrome $b_6f$ complex of oxygenic photosynthesis protects against oxygen damage. *J. Biol. Chem.* 274:1581-1587.

Zhang H., G. Kurisu, J.L. Smith and W.A. Cramer. 2003. A defined protein-detergent-lipid complex for crystallization of integral membrane proteins: the cytochrome $b_6f$ complex of oxygenic photosynthesis. *Proc. Natl. Acad. Sci. U.S.A* 100:5160-5163.

Zhong D. and A.H. Zewail. 2001. Femtosecond dynamics of flavoproteins: charge separation and recombination in riboflavine (vitamin $B_2$)-binding protein and in glucose oxidase enzyme. *Proc. Natl. Acad. Sci. U.S.A* 98:11867-11872.

Zouni A., H.-T. Witt, J. Kern, P. Fromme, N. Krauß, W. Saenger and P. Orth. 2001. Crystal structure of photosystem II from *Synechococcus elongatus* at 3.8 Å resolution. *Nature* 409:739-743.